Inorganic Chemistry

pubs.acs.org/IC

Article

Polymorphism and Visible-Light-Driven Photocatalysis of Doped Bi_2O_3:M (M = S, Se, and Re)

Marcus Weber, Raul D. Rodriguez, Dietrich R.T. Zahn, Klaus Stöwe, and Michael Mehring*

Cite This: *Inorg. Chem.* 2022, 61, 1571−1589

Read Online

ABSTRACT: δ-Bi_2O_3:M (M = S, Se, and Re) with an oxygen-defective *fluorite*-type structure is obtained by a coprecipitation method starting from the bismuth oxido cluster $[Bi_{38}O_{45}(OMc)_{24}(dmso)_9]\cdot 2dmso\cdot 7H_2O$ (**A**) in the presence of additives such as Na_2SO_4, Na_2SeO_4, NH_4ReO_4, $Na_2SeO_3\cdot 5H_2O$, and Na_2SO_3. The coprecipitation of the starting materials with aqueous NaOH results in the formation of alkaline reaction mixtures, and the cubic bismuth(III)-based oxides $Bi_{14}O_{20}(SO_4)$ (**1c**), $Bi_{14}O_{20}(SeO_4)$ (**2c**), $Bi_{14}O_{20}(ReO_{4.5})$ (**3c**), $Bi_{12.25}O_{16.625}(SeO_3)_{1.75}$ (**4c**), and $Bi_{10.51}O_{14.765}(SO_3)_{0.49}(SO_4)_{0.51}$ (**5c**) are obtained after microwave-assisted heating; formation of compound **5c** is the result of partial oxidation of sulfur. The compounds **1c**, **2c**, **4c**, and **5c** absorb UV light only, whereas compound **3c** absorbs in the visible-light region of the solar spectrum. Thermal treatment of the as-prepared metastable bismuth(III) oxide chalcogenates **1c** and **2c** at T = 600 °C provides a monotropic phase transition into their tetragonal polymorphs $Bi_{14}O_{20}(SO_4)$ (**1t**) and $Bi_{14}O_{20}(SeO_4)$ (**2t**), while compound **3c** is transformed into the tetragonal modification of $Bi_{14}O_{20}(ReO_{4.5})$ (**3t**) after calcination at T = 700 °C. Compounds of the systems $Bi_2O_3{-}SO_x$ (x = 2 and 3) and $Bi_2O_3{-}Re_2O_7$ are thermally stable up to T = 800 °C, whereas compounds of the system $Bi_2O_3{-}SeO_3$ completely lose SeO_3. Thermal treatment of **4c** and **5c** in air results in the oxidation of the tetravalent to hexavalent sulfur and selenium, respectively, upon heating to T = 400−500 °C. The as-prepared cubic bismuth(III)-based oxides **1c**−**5c** were studied with regard to the photocatalytic decomposition of rhodamine B under visible-light irradiation with compound **3c** showing the highest turnover and efficiency.

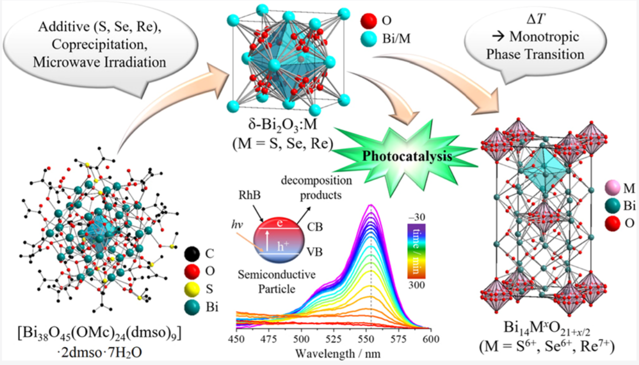

1. INTRODUCTION

Bismuth(III) oxide shows a distinctive polymorphism with eight well-characterized modifications to date: monoclinic α-Bi_2O_3,[1] tetragonal β-Bi_2O_3,[1] cubic γ-Bi_2O_3,[2] cubic δ-Bi_2O_3,[3] triclinic ω-Bi_2O_3,[4] trigonal η-Bi_2O_3,[5,6] orthorhombic ε-Bi_2O_3,[7] and monoclinic R-Bi_2O_3.[6] The latter is reported to be a "relaxed" intermediate phase that occurs during transition from η-Bi_2O_3 into α-Bi_2O_3.[6] In addition, the existence of ζ-Bi_2O_3 was postulated based on powder X-ray diffraction (PXRD) data.[8] Cubic δ-Bi_2O_3 represents the metastable high-temperature (HT) modification that exists in a quite narrow temperature range T = 717−824 °C.[3] The δ-modification of bismuth(III) oxide crystallizes in the space group $Fm\bar{3}m$ with an oxygen-defective CaF_2-type lattice.[3] Both the oxygen-defective lattice[9] and the polarizability of the $6s^2$ lone pair of electrons of the bismuth(III) cation[10] in δ-Bi_2O_3 contribute to the high oxygen ion conductivity. Therefore, the δ-phase is known as the best oxygen ion-conducting ceramic, making it suitable as a solid electrolyte[11−14] and as a gas sensing material.[15−17] Furthermore, some reports focus on the application of δ-Bi_2O_3 as an adsorbent for water purification.[18−21] More recently, the cubic δ-modification of bismuth(III) oxide came into focus as a semiconductor in photocatalytic processes[22−27] despite its lower efficiency compared to that of tetragonal β-Bi_2O_3.[28−30] In addition, δ-Bi_2O_3 was also investigated as a vanadium-stabilized phase (δ-$Bi_{11}VO_{19}$),[31−35] in combination with a cocatalyst (i.e., δ-Bi_2O_3-Ag),[36] and in composites such as AgX/δ-Bi_2O_3 (X = Br,[37] I[38]), δ-$Bi_2O_3/Bi_2O_2CO_3$,[39] and δ-Bi_2O_3/Bi_2MoO_6.[40] Thus, a plethora of synthetic approaches for δ-Bi_2O_3 in the form of powders,[18−22,24,26,27,39−41] films,[23,42−47] nanosheets,[25] and nanowires[48] was developed. However, stabilization of pure δ-Bi_2O_3 at room temperature is still a challenge; therefore, the application of the metastable modification is restricted to a low number of examples.[49−52] Stabilization of δ-Bi_2O_3 to room temperature can be achieved by doping,[53] but it must be kept

Received: October 25, 2021
Published: January 4, 2022

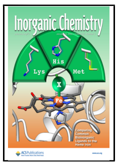

https://doi.org/10.1021/acs.inorgchem.1c03330
Inorg. Chem. 2022, 61, 1571−1589

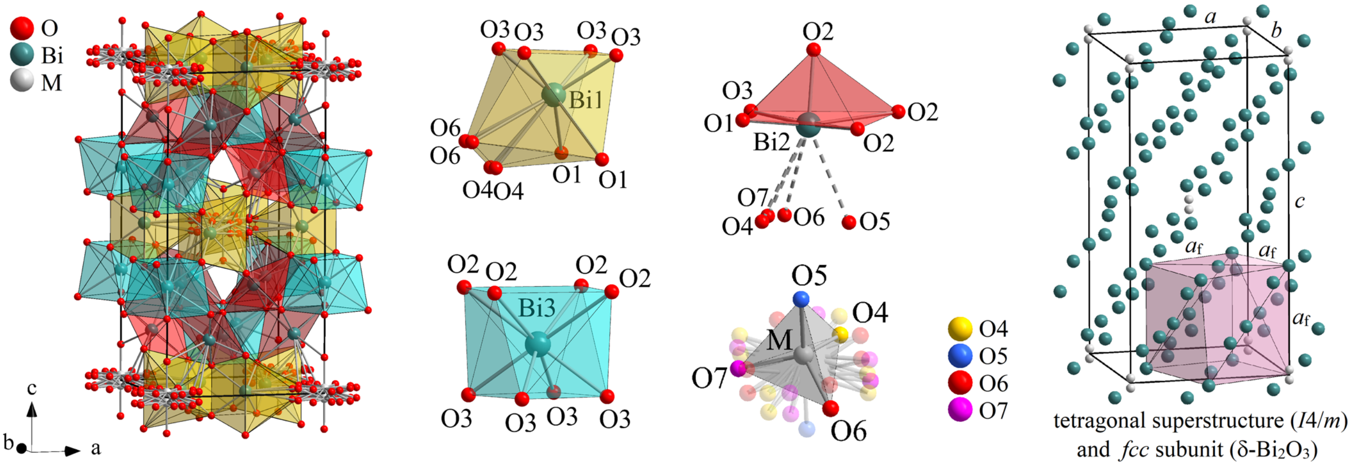

Figure 1. "Ball-and-stick" model (*left*) representing the general crystal structure of tetragonal Bi$_{14}$M^{x}O$_{21+x/2}$ (M = S,[99] Cr,[100,101] Mo,[101] and W[101] with x = +6; Re[102] with x = +7) with space group $I4/m$ in the solid state with the corresponding Bi−O and M−O coordination polyhedra (*middle*, Bi−O distances >2.9 Å are dashed). One possible tetrahedral orientation is shown for the [M^{x}O$_{1+x/2}$]$^{2-}$ group. The cation sublattice of Bi$_{14}$M^{x}O$_{21+x/2}$ (*right*) shows the structural relationship of the tetragonal superstructure to the *fluorite*-type subcell of δ-Bi$_2$O$_3$ (highlighted in pink). Based on drawings and structural data of tetragonal Bi$_{14}$O$_{20}$(CrO$_4$) with permission from references 100 (Copyright 2000 Elsevier) and 101 (Copyright 2003 Elsevier).

in mind that incorporation of dopants into the crystal lattice of bismuth(III) influences the physical properties and, for example, reduces the oxygen ion conductivity by several orders of magnitude.[10,54−56] In the last decades, numerous reports have dealt with the stabilization of δ-Bi$_2$O$_3$ using a variety of main-group elements and transition metals (B,[14] P,[57] Ti,[58,59] V,[31−34] Fe,[60] Y,[61,62] Nb,[62,63] Te,[64] Ta,[65] Ce,[66−68] Eu,[69] Tb,[70] Dy,[71,72] Er,[73−75] Tm,[76] Yb,[77,78] Lu,[79] and Th[80]) and double-doping (Hf/Zr,[81] Te/V,[82] Y/Yb,[83] Er/Nb,[84] Er/Gd,[85] Ho/Gd,[86] Ho/Dy,[87] Dy/W,[88] Sm/Ce,[89] Sm/Yb,[90] La/Mo,[91] Pr/Mo,[92] Dy/Tm,[93] Gd/Lu,[94,95] Yb/Dy,[96,97] Eu, or Tb/Th[98]). Compounds with the composition Bi$_{14}$M^{x}O$_{21+x/2}$ (M = S,[99] Cr,[100,101] Mo,[101] W[101] with x = +6; Re[102] with x = +7) exhibit tetragonal symmetry with the space group $I4/m$ (crystal structure illustrated in Figure 1).[99,101,102] The tetragonal unit cell of Bi$_{14}$M^{x}O$_{21+x/2}$ with the lattice parameters "a" and "c" represents a superstructure related to a *fluorite*-type subcell of δ-Bi$_2$O$_3$ (a_f) with $a = (\sqrt{10/2})\cdot a_f$ and $c = 3\cdot a_f$ (Figure 1).[99,102]

Among them, Bi$_{14}$WO$_{24}$ is the only ternary example, for which a cubic modification was additionally reported.[103,104] In the case of compounds related to Bi$_{14}$ReO$_{24.5}$, the cubic δ-phase is reported for quaternary compounds with the composition Bi$_{12.5}$Ln$_{1.5}$ReO$_{24.5}$ (Ln = Y,[12,105] La,[12,105,106] Pr,[106] Nd,[12,105] Sm,[107] Eu,[12] Gd,[108] Dy,[109] Ho,[110] Er,[12,111,112] Yb,[113] and Lu[112,114,115]). Semi and nonmetal-stabilized δ-Bi$_2$O$_3$ is only known for the binary systems of Bi$_2$O$_3$−B$_2$O$_3$[14] and Bi$_2$O$_3$−BiPO$_4$, respectively.[57] Several compounds of the binary system Bi$_2$O$_3$−SO$_3$ such as Bi$_{14}$O$_{20}$(SO$_4$),[99] Bi$_8$O$_{11}$(SO$_4$),[116] Bi$_9$O$_{12.5}$(SO$_4$),[117] and Bi$_{15}$O$_{21.5}$(SO$_4$)[117] exhibit a *fluorite*-related superstructure, but corresponding cubic modifications are still unknown to date. It is noteworthy that Bi$_{14}$ReO$_{24.5}$ is the only known example for this composition with a substituting heptavalent cation providing an interesting charge balancing mechanism including the incorporation of [ReO$_4$]$^-$ and [ReO$_6$]$^{5-}$ anions in a 3:1 ratio providing [ReO$_{4.5}$]$^{2-}$.[102] The parent geometry of the [Bi(3)O$_8$] group is a cube which is slightly rotated along one 4-fold axis toward an Archimedean antiprism resulting in four short and four long Bi(3)−O bonds.[100] Taking into account the 6s^2 electron lone pair of bismuth (e) extended along the 4-fold axis of the [Bi(3)O$_8$] polyhedra, the repulsion of the O(2) anions leads to a specific geometry. The Bi(2) cation forms a distorted axially compressed tetragonal pyramid with additional long-bonded oxide anions ($d_{\mathrm{Bi-O}} \approx 2.9$ Å).[100] The substituting cation "M" on the C$_4$ axis is disordered over two neighboring positions above and below the mirror plane (Figure 1). Orientational disorder is assumed for the coordinating oxide anions concentrated at the mirror plane except for those located on the C$_4$ axis providing a *pseudo*-octahedral geometry of the [M^{x}O$_{1+x/2}$]$^{2-}$ group.[100,101]

In a previous study, the formation of Bi$_{11}$VO$_{19}$—a ternary compound which is isostructural to δ-Bi$_2$O$_3$—was demonstrated by the coprecipitation method starting from the bismuth oxido cluster [Bi$_{38}$O$_{45}$(OMc)$_{24}$(dmso)$_9$] ($^-$OMc = $^-$O$_2$CC$_3$H$_5$) in the presence of NH$_4$VO$_3$ with aqueous NaOH followed by microwave-assisted heating.[118] Additionally, we briefly reported on the synthesis of sulfur- and selenium-doped δ-Bi$_2$O$_3$ with dopants in different oxidation states.[118] In this work, we report in detail the straightforward synthesis route toward δ-Bi$_2$O$_3$:M (M = S, Se, Re) via the above-mentioned coprecipitation method starting from the polynuclear bismuth oxido cluster **A** in the presence of sulfur-, selenium-, and rhenium-containing additives under alkaline conditions and microwave-assisted heating. The characterization (i.e., PXRD and Rietveld refinement) of the as-prepared cubic compounds with an oxygen-defective *fluorite*-type structure is discussed. Thermal stability and polymorphism are investigated by thermogravimetry (TG) and differential scanning calorimetry (DSC), PXRD, and Raman spectroscopy. The photocatalytic decomposition of aqueous rhodamine B (RhB) in the presence of δ-Bi$_2$O$_3$:M (M = S, Se, and Re) powders under visible-light irradiation is demonstrated.

2. EXPERIMENTAL SECTION

2.1. General. The precursor [Bi$_{38}$O$_{45}$(OMc)$_{24}$(dmso)$_9$]·2dmso·7H$_2$O (**A**) was prepared according to a previously reported procedure.[119] Na$_2$SeO$_4$ and Na$_2$SeO$_3$·5H$_2$O were purchased from Sigma-Aldrich and VWR, respectively. Na$_2$SO$_4$, Na$_2$SO$_3$, and NH$_4$ReO$_4$ were purchased from Alfa Aesar. The aqueous NaOH solutions were prepared in plastic beakers to ensure silicate-free conditions; otherwise, contamination of bismuth(III) oxide with silicates favors the formation of the *sillenite*-type compound $Bi_{12}SiO_{20}$, which cannot be separated from δ-Bi_2O_3:M (M = S, Se, Re).[120,121] Silver sheets (99.9%) were purchased from ChemPur. Collected powders were stored in resealable microvessels (V = 1.5 mL, polypropylene) purchased from Eppendorf AG. A HI 223 Calibration Check pH meter (Hanna Instruments) was used to measure pH values of the as-prepared reaction mixtures. The subsequent microwave-assisted heating was carried out using a microwave Discover-S DC 5061 (CEM MATTHEWS, NC) in Pyrex-vessels equipped with PTFE-linings (V = 35 mL), and a special atmosphere was not required. The heating procedure was carried out with a power of P = 60 W and the setpoint temperature was achieved within t = 5 min. The cooling procedure was performed within t = 2 min using compressed air. PXRD was carried out with a STOE STADI P diffractometer (Darmstadt, Germany) using Cu$K\alpha_1$ radiation (λ = 1.54056 Å, U = 40 kV, and I = 40 mA) and a Ge(111)-monochromator. The full width at half maximum (FWHM) was corrected for instrumental broadening using a LaB_6 standard (SRM 660) purchased from NIST. The value of β was corrected from the following equation:

$$\beta^2 = \beta^2{}_{\text{measured}} - \beta^2{}_{\text{instrument}} \tag{1}$$

where $\beta^2{}_{\text{measured}}$ and $\beta^2{}_{\text{instrument}}$ are the FWHM of measured and standard profiles. Rietveld refinement of the PXRD patterns was carried out using the TOPAS program (Version 5.0 from Bruker Corp., Germany).[122] TG/DSC experiments were carried out with a Mettler Toledo TGA/DSC1 1600 system with an MX1 balance. The measurements were performed in Al_2O_3 crucibles from T = 30 to 800 °C with a heating rate of ΔT = 10 K·min^{-1} in an air flow ($\dot{V}_{\text{air}}$ = 20 mL·min^{-1}) and hold time of t = 60 min followed by subsequent cooling (ΔT = 2.5 K·min^{-1}) to T = 40 °C. Specific surface analyses were performed using N_2 adsorption−desorption isotherms at liquid nitrogen temperature (T = 77 K) using a Micromeritics Gemini 2370. They were evaluated by the Brunauer−Emmett−Teller (BET) method in the p/p_0 range of 0.001−0.25. The particle size distribution (PSD) was determined using a Zetasizer Nano ZS (Malvern Instruments) with dynamic light scattering (DLS). Using laser light (λ = 633 nm, P = 4 mW) as a light source, suspensions with a size range from 0.6 nm to 6 μm can be investigated. The analyses were performed at an angle of 173 ° (noninvasive backscatter (NIBS) default). The powders were dispersed in deionized water (β = 1.0 g·L^{-1}) and ultrasonicated (f = 35 kHz, t = 1 min), filled into glass cuvettes (DTS0012), and measured at T = 25 °C. The calculation of the PSD was automatically performed following the "Mie theory" assuming spherical particles. Attenuated total reflectance Fourier transform infrared spectroscopy (ATR-FTIR) was performed using an FTS-165 spectrometer. UV−vis spectroscopy was performed using a Cary 60 UV−vis (Co. Agilent Technologies) equipped with a Barrelino (Co. Harrick Scientific Products) remote diffuse reflection probe. The band-gap determination of the semiconductors was carried out via the approach of Tauc et al. using optical absorbance data.[123] After further development by Davis and Mott,[124] the "Tauc model" is based on an energy-dependent absorption coefficient α expressed by the following formula:[123−127]

$$\alpha h\nu = A(h\nu - E_g)^{n/2} \tag{2}$$

where α is the absorption coefficient, h is the Planck constant, ν is the photon frequency, E_g is the band-gap energy, and A is a proportionality constant. The parameter n defines the type of electron transfer in the semiconductor with n = 4 for indirect allowed and n = 1 for direct allowed electronic transitions.[127] Plotting $(\alpha h\nu)^{2/n}$ against $h\nu$ provides the corresponding Tauc plot, and a linear regression line is used to determine the band-gap energy E_g. The band-gap energy is usually determined from diffuse reflectance spectra; by applying the Kubelka−Munk function,[128,129] these data can be transformed into the corresponding absorption spectra:[130]

$$F(R_\infty) = K/S = (1 - R_\infty)^2/2R_\infty \tag{3}$$

where $R_\infty = R_{\text{sample}}/R_{\text{standard}}$ is the reflectance of an infinitely thick specimen, K is the absorption coefficient, and S is the scattering coefficient.[129] Replacing of α in eq 2 by $F(R_\infty)$ results in:[130]

$$F(R_\infty)h\nu = A(h\nu - E_g)^{n/2} \tag{4}$$

A scanning electron microscope (SEM, NanoNovaSEM, Co. FEI, OR, USA) was used for the energy-dispersive X-ray (EDX) spectroscopy experiments. Elemental analysis for carbon, hydrogen, nitrogen, and sulfur (CHNS) was performed using a "Vario EL" (Heraeus). Raman spectra were recorded using a Raman spectrometer Horiba LabRam HR800, the laser excitation of a solid-state laser (λ = 514.7 nm) or a gas laser (λ = 632.8 nm) was focused on the sample with a 50× long working distance objective (N.A. 0.5). The scattered Raman signal was collected in the backscattering geometry and analyzed by a diffraction grating with 600 lines/mm. Temperature-controlled experiments were performed by placing the sample on a Linkam TC91 stage (Linkam Scientific Instruments Ltd., Surrey, England). The temperature was changed from room temperature up to T = 600 °C. The photodegradation experiments were carried out in a water-cooled glass reactor (T = 15 °C). The as-prepared samples (m = 40 mg) were dispersed in an aqueous solution of rhodamine B (RhB, V = 40 mL, c = 10 μmol·L^{-1}, pH = 4.7 at T = 15 °C[131]) and stirred in the dark for t = 30 min. The suspension was illuminated with a xenon lamp (type Cermax VQTM ME300BF, Co. PerkinElmer, P = 300 W) equipped with a hot mirror ($\lambda \leq$ 700 nm) and a UV cutoff filter ($\lambda \geq$ 420 nm, GG420, Co. Schott) to provide only visible light. The UV−vis measurements were carried out by stopping to stir and switching off the lamp followed by centrifugation of a withdrawn sample (V = 5 mL). After the measurement, the solid was suspended and refilled into the main reactor. The measurements were carried out with a 10 min interval up to 60 min, 15 min interval up to 120 min, and a 30 min interval up to 300 min. The degree of conversion is determined by calculating the area under the UV−vis curve between λ = 450 and 600 nm and plotted as a function of irradiation time.

2.2. Synthesis of δ-Bi_2O_3:M (M = S, Se, and Re; 1c−5c). In a PTFE-lined vessel, the bismuth oxido cluster **A** (m = 250 mg and n = 0.021 mmol) was dissolved in EtOH (V = 2.5 mL) under stirring, and an aqueous solution of Na_2SO_4 (c = 1.64 M, V = 0.14 mL; **L1**), Na_2SeO_4 (c = 2.43 M, V = 0.14 mL; **L2**), $Na_2SeO_3 \cdot 5H_2O$ (c = 1.64 M, V = 0.14 mL; **L3**), or Na_2SO_3 (c = 2.56 M, V = 0.18 mL; **L4**) was added; NH_4ReO_4 was added as a solid material (m = 85 mg, n = 0.32 mmol, **S1**). After addition of the aqueous NaOH solution (c = 0.5 M, V = 1.4 mL for **L1**−**L4** and V = 1.6 mL for **S1**) under vigorous stirring, a colorless precipitate was formed immediately in the presence of **L1**−**L4**; a yellow precipitate was formed in the presence of **S1**. The PTFE-lined vessel was closed and transferred into the microwave reactor followed by heating of the alkaline reaction mixture (pH = 13.6 (**L1**), 13.3 (**L2**), 13.2 (**L3**), and 13.2 (**L4**)) to T = 100 °C for t = 10 min; the mixture containing **S1** (pH = 12.7) was heated to T = 100 °C for t = 1 min. After cooling to room temperature using compressed air, the as-prepared solid was collected by centrifugation (f_{rot} = 3000 min^{-1}, t = 1 min), washed with EtOH/water (V:V = 1:1) and three times with water, and dried under vacuum (p = 10^{-3} mbar) for t = 60 min (T = 60 °C). Details are listed in Table 1 (yield η is based on bismuth in **A**).

To remove β-Bi_2O_3, the as-prepared mixture consisting of $Bi_{14}O_{20}(ReO_{4.5})$ (**3c**) and β-Bi_2O_3 (m = 587 mg) was dispersed in deionized H_2O (V = 10 mL) and ultrasonicated (f = 35 kHz) for t = 10 min. The suspension was centrifuged (f_{rot} = 1000 min^{-1}, t = 1

Table 1. Products of the Coprecipitation Approaches

additive	product	m/mg	η/%
L1	$Bi_{14}O_{20}(SO_4)$ (**1c**)	172	90
L2	$Bi_{14}O_{20}(SeO_4)$ (**2c**)	175	90
S1	$Bi_{14}O_{20}(ReO_{4.5})$ (**3c**) + β-Bi_2O_3	167	86
L3	$Bi_{12.25}O_{16.625}(SeO_3)_{1.75}$ (**4c**)	174	86
L4	$Bi_{10.51}O_{14.765}(SO_3)_{0.49}(SO_4)_{0.51}$ (**5c**)	180	95

https://doi.org/10.1021/acs.inorgchem.1c03330

min), and the supernatant dispersion (enriched with **3c**) was separated from the resulting residue (enriched with β-Bi_2O_3, **C1**) by decanting into a new centrifuge tube. This procedure was repeated several times to ensure the complete separation of β-Bi_2O_3 evaluated by PXRD analysis of the resulting residues **C2**−**C5** (Figure S1, details are listed in Table 2).

Table 2. Details of the Purification Procedure by Centrifugation of 3c + β-Bi_2O_3 Dispersed in Water

residue	f_{rot}/min^{-1}	t/min	m/mg	residue composition (PXRD)
C1	1000	1	301	$Bi_{14}O_{20}(ReO_{4.5})$ + β-Bi_2O_3
C2	1000	1	25	$Bi_{14}O_{20}(ReO_{4.5})$ + β-Bi_2O_3
C3	1000	1	25	$Bi_{14}O_{20}(ReO_{4.5})$
C4	1000	1	17	$Bi_{14}O_{20}(ReO_{4.5})$
C5	1000	1	15	$Bi_{14}O_{20}(ReO_{4.5})$
C6	4000	10	175	$Bi_{14}O_{20}(ReO_{4.5})$ (**3c**)

The final centrifugation step (f_{rot} = 4000 min^{-1}, t = 10 min) was carried out to completely retrieve the remaining particles of compound **3c** from the dispersion medium (H_2O). After drying under vacuum (p = 10^{-3} mbar) for t = 60 min (T = 60 °C), the residue **C6** consists of $Bi_{14}O_{20}(ReO_{4.5})$ (m = 175 mg, n = 4.99 mmol, η = 30% based on initial mass of the mixture of **3c** and β-Bi_2O_3) and is labeled as compound **3c**.

2.3. Thermal Treatment of δ-Bi_2O_3:M (M = S, Se, and Re). The as-prepared solids **1c**−**5c** were placed on a silver sheet and transferred to a tubular furnace under air flow ($\dot{V}_{air}$ = 50 L·h^{-1}). After heating to the appropriate temperature (ΔT = 10 K·min^{-1}), the setpoint temperature was held for t = 60 min followed by cooling to room temperature (ΔT = 2.5 K·min^{-1}). The as-obtained solids were collected and analyzed by PXRD (Table S1).

3. DISCUSSION

3.1. Synthesis and Characterization of δ-Bi_2O_3:M (M = S, Se, and Re). Based on the preliminary results of our former work,[118] the coprecipitation of the bismuth oxido cluster **A** in the presence of Na_2SO_4 (**L1**), Na_2SeO_4 (**L2**), NH_4ReO_4 (**S1**), $Na_2SeO_3\cdot 5H_2O$ (**L3**), and Na_2SO_3 (**L4**) with aqueous NaOH results in the formation of compounds with the δ-Bi_2O_3 structure (space group $Fm\bar{3}m$) and the composition $Bi_{14}M^xO_{21+x/2}$ (M = S^{6+} (**1c**), Se^{6+} (**2c**), x = 6; Re^{7+} (**3c**), x = 7), $Bi_{12.25}O_{16.625}(SeO_3)_{1.75}$ (**4c**), and $Bi_{10.51}O_{14.765}(SO_3)_{0.49}(SO_4)_{0.51}$ (**5c**). Structural data are based on refined PXRD data (Figure 2, Table 3; refined atomic positions and occupancies see Table S2).

The postulated formulas are confirmed by EDX-analysis (Figure S2, Table S3). However, we were not able to synthesize pure $Bi_{14}O_{20}(ReO_{4.5})$ (**3c**) by varying the reaction parameters (i.e., Bi/Re ratio, volume, and concentration of the NaOH solution, reaction temperature, and time) and the as-prepared precipitate did always contain β-Bi_2O_3 as a by-product. The latter was removed by a centrifugation procedure based on the higher density of binary β-Bi_2O_3 (D_x = 9.17 g·cm^{-3})[137] compared to the ternary $Bi_{14}O_{20}(ReO_{4.5})$ (D_x = 8.62 g·cm^{-3}) and gave the pure compound **3c** after several steps (Figure S1, Table 2). The most common accepted structure of δ-Bi_2O_3 is based on the refinements of Battle et al.[132] and the theoretical calculations by Yashima and Ishimura[133] confirming δ-Bi_2O_3 as a highly defective *fluorite*-type structure. It is noteworthy that the Willis model of δ-Bi_2O_3 provides a more differentiated view on the oxide anion sublattice in δ-Bi_2O_3 by assuming a higher degree of disorder on the ideal 8*c* Wyckoff positions resulting in the occupation of additional 32*f* positions by oxygen atoms.[134−136] The refinement of the PXRD patterns of the compounds **1c**−**5c** reveals the statistical occupation of the 4*a* Wyckoff positions by Bi^{3+} and the corresponding cationic dopants. The oxygen atoms O1 and O2 are located on the 8*c* and 32*f* Wyckoff positions in accordance with the above-mentioned models,[47,132−136] resulting in Bi−O bond distances in the range of d_{Bi-O} = 2.26−2.44 Å for **1c**−**5c** (Table 3). The oxygen atom O3 occupies an additional 32*f* position and is involved in the M−O bonds (M = S in **1c**, **5c**; Se in **2c**, **4c**; Re in **3c**, respectively, Table 3).

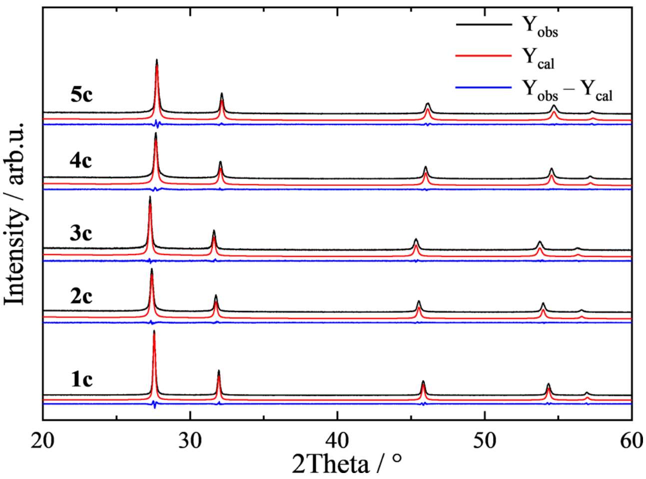

Figure 2. Refined PXRD patterns of δ-Bi_2O_3:M (M = S, Se, Re; **1c**−**5c**) based on the crystal structure of cubic δ-Bi_2O_3 ($Fm\bar{3}m$).[132−136]

The lattice parameters "a_f" and thus the cell volumes "V_f" of the cubic compounds **1c**, **2c**, and **3c** increase in accordance with the ionic radius "r_{ion}" of the dopants "M" ($r_{ion}(S^{6+})$ = 0.29 Å < $r_{ion}(Se^{6+})$ = 0.42 Å < $r_{ion}(Re^{7+})$ = 0.53 Å; CN = 6),[138] which are incorporated into the δ-Bi_2O_3-type lattice with the same quantities (Bi/M = 14:1). Compared to compounds **1c**−**3c**, the bismuth(III)-based oxides **4c** and **5c** exhibit significantly decreased cell parameters because of the increasing content of S^{4+} and Se^{4+} in the cation sublattice. These dopants exhibit a significantly larger ionic radius ($r_{ion}(S^{4+})$ = 0.37 Å, $r_{ion}(Se^{4+})$ = 0.50 Å) compared to hexavalent sulfur and selenium cations in **1c** and **2c** (Table 3).[138] However, the lower values for the unit cell length "a_f" and the cell volume "V_f" of **4c** and **5c** compared to **1c** and **2c** are caused by the replacement of the even larger bismuth(III) cations (r_{ion} = 1.03 Å, CN = 6)[138] by selenium(IV) and mixed valent sulfur(IV/VI, Table 3). The cubic compound $Bi_{14}O_{20}(ReO_{4.5})$ (**3c**) with an oxygen-defective *fluorite*-type structure represents a rare-earth-free compound of the previously reported $Bi_{12.5}Ln_{1.5}ReO_{24.5}$ (Figure 3).[12,105−115] The unit cell length of $Bi_{14}O_{20}(ReO_{4.5})$ (**3c**) with a_f = 5.6469(3) Å is very close to that of $Bi_{12.5}La_{1.5}ReO_{24.5}$ with a_f = 5.6456(3) Å because of the similar ionic radii of Bi^{3+} (r_{ion} = 1.03 Å, CN = 6) and La^{3+} (r_{ion} = 1.032 Å, CN = 6).[138] The substitution of $Bi_{12.5}Ln_{1.5}ReO_{24.5}$ with lanthanides of lower ionic radii results in a decrease of the unit cell length "a_f" in accordance with the lanthanoid contraction (Figure 3).[12,105−115] The incorporation of the dopants into the δ-Bi_2O_3-type lattice of the compounds **1c**−**5c** is confirmed by IR- and Raman spectroscopy (Figures 4 and 5). In the IR spectra, cubic $Bi_{14}O_{20}(SO_4)$ (**1c**) and $Bi_{14}O_{20}(SeO_4)$ (**2c**) show characteristic vibration bands for the corresponding chalcogenate groups ($[SO_4]^{2-}$: 1057 cm^{-1} (ν_3), 962 cm^{-1} (ν_1), and 599 cm^{-1} (ν_4);[117,139] $[SeO_4]^{2-}$: 836 cm^{-1}(ν_1)[140]). For

Table 3. Refined Lattice Parameters and Bond Distances of $Bi_{14}O_{20}(SO_4)$ (**1c**), $Bi_{14}O_{20}(SeO_4)$ (**2c**), $Bi_{14}O_{20}(ReO_{4.5})$ (**3c**), $Bi_{12.25}O_{16.625}(SeO_3)_{1.75}$ (**4c**), and $Bi_{10.51}O_{14.765}(SO_3)_{0.49}(SO_4)_{0.51}$ (**5c**) Based on the Crystal Structure of δ-Bi_2O_3 ($Fm\bar{3}m$)[132−136]

	1c	2c	3c	4c	5c
r_{ion} (M)[a]/Å	0.29	0.42	0.53	0.50	0.37/0.29
a/Å	5.5899(1)	5.6272(3)	5.6469(3)	5.5730(3)	5.5569(3)
V/Å^3	174.67(1)	178.19(3)	180.06(3)	173.09(3)	171.60(3)
d_{Bi1-O1}/Å	2.4205(1)	2.4367(1)	2.4452(1)	2.4132(1)	2.4062(1)
d_{Bi1-O2}/Å	2.2829(4)	2.305(2)	2.305(2)	2.281(2)	2.269(3)
d_{M1-O3}/Å	1.43(18)	1.37(12)	2.1(4)	1.82(15)	1.5(2)
wt % Rietveld	100	100	100	100	100
d_p/nm	247(9)	65.2(10)	230(20)	63.2(11)	680(140)
D_x/g·cm^{-3}	8.470(1)	8.4210(13)	8.6169(13)	8.3552(15)	8.4774(14)
R_{wp}/%	7.83	4.72	6.83	5.22	5.79
R_{Bragg}	0.612	0.477	0.272	0.700	0.430

[a] Ionic radius of the dopant "M" (S^{4+}, S^{6+}, Se^{4+}, Se^{6+}, Re^{7+}) with a coordination number (CN) of 6.[138]

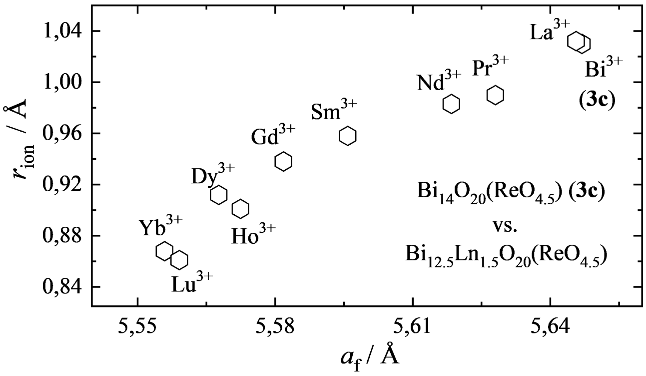

Figure 3. Correlation between the ionic radius "r_{ion}" of Ln^{3+} (Ln = La, Pr, Nd, Sm, Gd, Dy, Ho, and Lu; CN = 6)[138] and the cell parameter "a_f" in cubic $Bi_{12.5}LnO_{20}(ReO_{4.5})$[12,105−115] in comparison to $Bi_{14}O_{20}(ReO_{4.5})$ (**3c**). Based on a diagram with permission from reference 107 (Copyright 2014 Elsevier) and reference 109 (Copyright 2012 Elsevier).

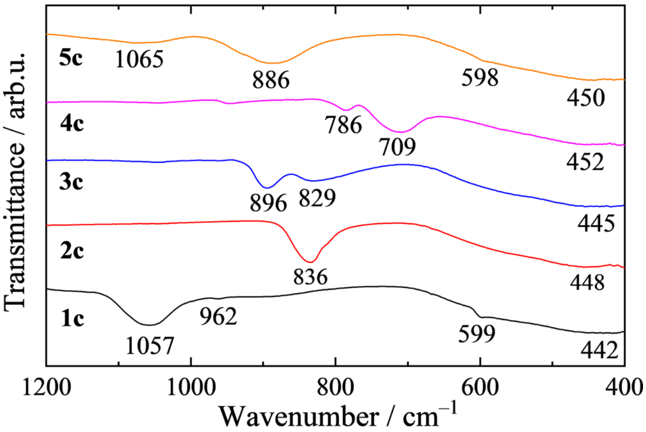

Figure 4. IR-spectra of δ-Bi_2O_3:M (M = S, Se, and Re; **1c**−**5c**).

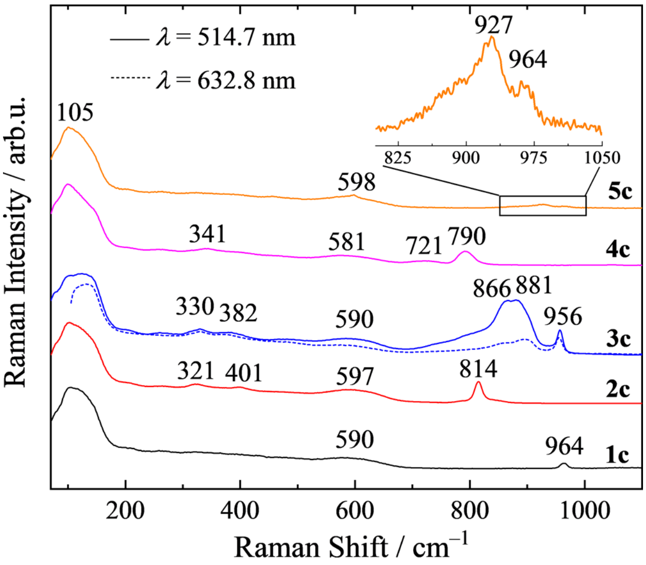

Figure 5. Raman spectra of δ-Bi_2O_3:M (M = S, Se, and Re; **1c**−**5c**) including the inset range from ν = 800 to 1050 cm^{-1} for **5c**.

$Bi_{14}O_{20}(ReO_{4.5})$, Crumpton et al. suggested the presence of tetrahedral $[ReO_4]^-$ with additional octahedral $[ReO_6]^{5-}$ groups (3:1 ratio; $[(ReO_4)_{0.75}(ReO_6)_{0.25}]^{2-} = [ReO_{4.5}]^{2-}$) to provide charge compensation.[102]

Thus, the mentioned perrhenate groups should be present in the as-prepared cubic modification of $Bi_{14}O_{20}(ReO_{4.5})$ (**3c**) as well as in the tetragonal polymorph.[102] Regular $[ReO_4]^-$ tetrahedra (symmetry T_d) exhibit four vibration modes denoted as ν_1 (A_1), ν_2 (E), ν_3 and ν_4 (T_2), and only the latter two modes are IR-active.[141] The ν_3 mode of the $[ReO_4]^-$ in **3c** is located at approx. 896 cm^{-1}. The vibration band at 829 cm^{-1} is assigned to the ν_1 (A_{1g}) mode of $[ReO_6]^{5-}$.[141,142] Thus, the IR spectrum of **3c** confirms the presence of both perrhenate groups, the tetrahedral $[ReO_4]^-$ and the octahedral $[ReO_6]^{5-}$, in agreement with the charge compensation mechanism suggested by Crumpton et al.[102] The presence of $[SeO_3]^{2-}$ groups in **4c** is confirmed by vibration bands at 786 cm^{-1} (ν_1) and 709 cm^{-1} (ν_3),[143,144] whereas the existence of both sulfite and sulfate groups in **5c** is verified by the vibration bands at 886 cm^{-1} ($\nu_1[SO_3]^{2-}$),[145] 1065 cm^{-1} ($\nu_3[SO_4]^{2-}$), and 598 cm^{-1} ($\nu_4[SO_4]^{2-}$), respectively.[117,139] The broad bands in the range of 442−452 cm^{-1} are assigned to the Bi−O vibrations in **1c**−**5c**.[146]

Raman spectra of compounds **1c**−**5c** were recorded in the range of ν = 70−1050 cm^{-1} (Figure 5). The Raman spectra of δ-Bi_2O_3:M (M = S, Se, Re; **1c**−**5c**) show intense and broad bands at approx. 100 cm^{-1}, which are indicative of external modes of the lattice vibrations in the unit cell.[147] Reference experiments on a silicon sheet show that the cutoff laser filter is not the origin of these low-frequency peaks (Figure S3). The internal modes in the range of 581−597 cm^{-1} are assigned to the Bi−O stretching vibrations of distorted $[BiO_6]$ polyhedra.[147] The sulfate group in **1c** shows a vibration band at 964 cm^{-1} (ν_1),[148,149] and the presence of the selenate group in **2c** is confirmed by bands located at 814 cm^{-1} (ν_1), 401 cm^{-1} (ν_4), and 321 cm^{-1} (ν_2).[140,150−153] Several vibration modes of the $[ReO_4]^-$ group in **3c** lead to the bands at 956 cm^{-1} (ν_1), 881 cm^{-1} (ν_3 B_g), 866 cm^{-1} (ν_3 E_g), 382 cm^{-1} (ν_4), and 330 cm^{-1} (ν_2).[154−156] The ν_1 Raman vibration mode of the $[ReO_6]^{5-}$ group at approx. 800 cm^{-1} is overlapped by the very broad vibration of the ν_3 mode ($[ReO_4]^-$), but the vibration mode at approx. 475 cm^{-1} is assigned to the ν_5 mode of the $[ReO_6]^{5-}$ group.[142,157] The $[SeO_3]^{2-}$ groups in **4c** cause vibration bands at 790 cm^{-1} (ν_1), 721 cm^{-1} (ν_3), and 341 cm^{-1} (ν_4).[143,150,152] The presence of mixed-valent sulfur in **5c** is confirmed by the vibration modes of the sulfite (927 cm^{-1} (ν_1) and 598 cm^{-1} (ν_2)) and sulfate group (964 cm^{-1} (ν_1)).[148,149] In comparison to the compounds **1c**, **2c**, **4c**, and **5c** of the systems Bi_2O_3−SO_x and Bi_2O_3−SeO_x ($2 \leq x \leq 3$), the ν_3 mode of $[ReO_4]^-$ in **3c** exhibits a significantly higher intensity when the Raman spectrum was recorded using a green laser (λ = 514.7 nm). This behavior is attributed to the different absorption properties of the as-prepared semiconductors. In the corresponding diffuse reflectance UV−vis spectra (Figure S4), the compounds **1c**, **2c**, **4c**, and **5c** exhibit an absorption edge in the UV region of the solar light spectrum with $\lambda \approx$ (430 ± 3) nm, whereas the bismuth(III) oxide perrhenate **3c** with $\lambda \approx$ (521 ± 2) nm absorbs visible light. Therefore, resonant excitation of the semiconductor **3c** by the green laser irradiation causes a significant increase in the intensity of the perrhenate group because of the *Resonance Raman Effect*.[158−160] Recording the Raman spectrum of **3c** with a red laser (λ = 632.8 nm) results in a significant decrease of the $[ReO_4]^-$ vibration bands because of the nonresonant excitation of the semiconductor. Based on the results from Raman spectroscopy, compound **3c** is concluded to be a visible-light-driven semiconductor, which might be suitable for photocatalytic decomposition of pollutants under visible-light irradiation (see chapter 3.3).

To date, some contradictory reports were published regarding δ-Bi_2O_3 to be a direct or an indirect semiconductor. Zayed reported on the physical properties of δ-Bi_2O_3 thin films, and the behavior of the absorption coefficient "α" in this work was indicative of an indirect electronic transition.[161] Depending on the film thickness, band-gap energy values in the range of 2.38−2.79 eV were reported.[161] The reports by Fan et al. dealt with thin films of δ-Bi_2O_3, too, and the cubic bismuth(III) oxide polymorph was characterized to be an indirect semiconductor as well with band-gap energies from 1.73 to 2.81 eV depending on the annealing temperature.[162,163] In the work by Zhou et al., Te^{4+}/V^{5+}-stabilized δ-Bi_2O_3 was characterized as an indirect allowed-type semiconductor with $E_g \approx$ 2.4−2.5 eV.[82] In contrast to the characterization of δ-Bi_2O_3 as an indirect semiconductor, Huang et al. carried out first-principles studies showing direct electronic transitions from the O 2p state in the valence band (VB) to the Bi 6p state in the conduction band (CB).[164] Former studies dealing with δ-Bi_2O_3 powders assumed direct allowed electronic transitions, and band-gap energies in the range of 3.01[28,35]−3.59 eV[39] were reported.

In the present work, the UV−vis spectra (Kubelka−Munk function[128,129]) of the as-prepared cubic bismuth(III) oxides reveal an extrapolated absorption edge in the range λ = (390 ± 3) nm to (403 ± 3) nm for compounds **1c**, **2c**, **4c**, and **5c** (Figure 6).

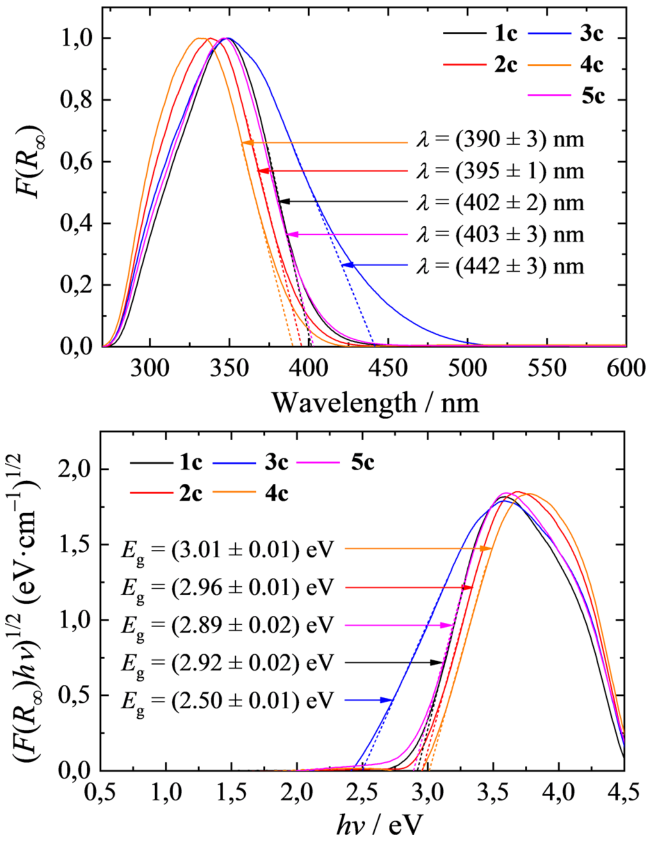

Figure 6. UV−vis absorption spectra (Kubelka−Munk function,[128,129] *top*) and Tauc plots[123,124,130] for the determination of the indirect band-gap energy E_g (*bottom*) of the as-prepared δ-Bi_2O_3:M (M = S, Se, and Re; **1c**−**5c**).

Similar to the diffuse reflectance UV−vis spectra (Figure S4), the bismuth(III) oxide perrhenate **3c** exhibits the highest value with λ = (442 ± 3) nm indicating the absorption of visible light, whereas the sulfur- and selenium containing compounds are limited to the UV-range of the solar spectrum. The extrapolated band-gap energies E_g of **1c**, **2c**, **4c**, and **5c** are in the range of (2.89 ± 0.02)−(3.01 ± 0.01) eV for indirect allowed electronic transitions (Figure 6); E_g values for direct allowed electronic transitions are in the range of (3.21 ± 0.02)−(3.34 ± 0.03) eV (Figure S5). For the bismuth(III) oxide perrhante **3c**, E_g values of (3.00 ± 0.03) and (2.50 ± 0.01) eV were determined for the direct and indirect band-gap energies, respectively. Concerning the findings of the Raman studies indicating the resonant excitation of cubic $Bi_{14}O_{20}(ReO_{4.5})$ (**3c**) by green laser irradiation (λ = 514.7 nm, corresponds to approx. 2.41 eV, Figure 5), compound **3c** is assumed to be an indirect semiconductor. Excitation of **3c** as a direct semiconductor ($E_g \approx$ 3 eV) by green laser irradiation can be neglected because of the huge energy difference of approx. 0.6 eV, whereas excitation of **3c** as an indirect semiconductor with $E_g \approx$ 2.5 eV seems to be more likely. Compounds **1c**, **2c**, **4c**, and **5c** cannot be excited by green laser irradiation, independent of being a direct ($E_g \approx$ 3.2 eV) or indirect semiconductor ($E_g \approx$ 2.9 eV).

The as-obtained powders of δ-Bi_2O_3:M (M = S, Se, and Re; **1c**−**5c**) consist of submicrometer particles with diameters in the range of d = 50−1000 nm based on PSD curves obtained from DLS studies on aqueous suspensions of **1c**−**5c** (Figure S6). N_2-adsorption studies on the powders of **1c**−**5c** revealed small specific surface areas with A_{BET} = 8 $m^2 \cdot g^{-1}$ (**1c**, and **2c**), 11 $m^2 \cdot g^{-1}$ (**3c**), 19 $m^2 \cdot g^{-1}$ (**4c**), and 11 $m^2 \cdot g^{-1}$ (**5c**).

After storage of $Bi_{14}O_{20}(SO_4)$ (**1c**), $Bi_{14}O_{20}(SeO_4)$ (**2c**), $Bi_{12.25}O_{16.625}(SeO_3)_{1.75}$ (**4c**), and $Bi_{10.51}O_{14.765}(SO_3)_{0.49}(SO_4)_{0.51}$ (**5c**) for 2 years in closed microvessels in air, the resulting aged compounds—labeled as **1c***, **2c***, **4c***, and **5c***, respectively—were analyzed by PXRD (Figure S7). The PXRD patterns of **1c*** and **2c*** reveal a slight carbonation of $Bi_{14}O_{20}(MO_4)$ (M = S and Se) confirmed by the detection of reflections assigned to $Bi_2O_2CO_3$, whereas the PXRD patterns of **4c*** and **5c*** solely contain reflections of the initial *fluorite*-type structure. It is known that bismuth(III) oxide is sensitive to CO_2 from air and also from water ($CO_2(aq)$) to give bismuth(III) oxide carbonate.[165] The resistance of **4c** and **5c** against the reaction with CO_2 to $Bi_2O_2CO_3$ is attributed to the higher content of selenium(IV) and sulfur(IV/VI) cations replacing the trivalent bismuth cations in the *fluorite*-type lattice in contrast to the bismuth(III) oxide chalcogenates **1c** and **2c**.

3.2. Investigations on Polymorphism and Thermal Stability of Bi_2O_3:M (M = S, Se, and Re).

Calcination of cubic $Bi_{14}O_{20}(SO_4)$ (**1c**) at T = 600 °C and $Bi_{14}O_{20}(ReO_{4.5})$ (**3c**) at T = 700 °C on a silver sheet results in the formation of the corresponding known tetragonal polymorphs $Bi_{14}O_{20}(SO_4)$ (**1t**)[99] and $Bi_{14}O_{20}(ReO_{4.5})$ (**3t**)[102] with the space group $I4/m$ (Figure 7, Table 4). Francesconi et al. and Crumpton et al. reported first on the synthesis and characterization of the tetragonal modifications of $Bi_{14}O_{20}(SO_4)$ and $Bi_{14}O_{20}(ReO_{4.5})$, obtained from solid-state reactions of α-Bi_2O_3 with $(NH_4)_2SO_4$ and NH_4ReO_4, respectively, at T = 750–800 °C.[99,102] The new tetragonal modification of $Bi_{14}O_{20}(SeO_4)$ (**2t**) is formed after calcination of cubic $Bi_{14}O_{20}(SeO_4)$ (**2c**) on a silver sheet at T = 600 °C. The compositions of the as-obtained residues were confirmed by evaluation of the EDX spectra (Figure S8 and Table S4). The crystal structure of the tetragonal compounds **1t**–**3t** with lattice parameters "a" and "c" represents a superstructure related to a cubic *fluorite*-type subcell with unit cell length "a_f" by the correlation $a = (\sqrt{10}/2) \cdot a_f$ and $c = 3 \cdot a_f$.[99,102] The unit cell length values of the cubic (**1c**–**3c**; Table 3) and tetragonal compounds (**1t**–**3t**; Table 4) are in accordance with this correlation.[99,102] Similar to the corresponding cubic modifications, the unit cell parameters "a," "c," and "V" of **1t**–**3t** increase in accordance with the ionic radius of the incorporated cations (Table 4).

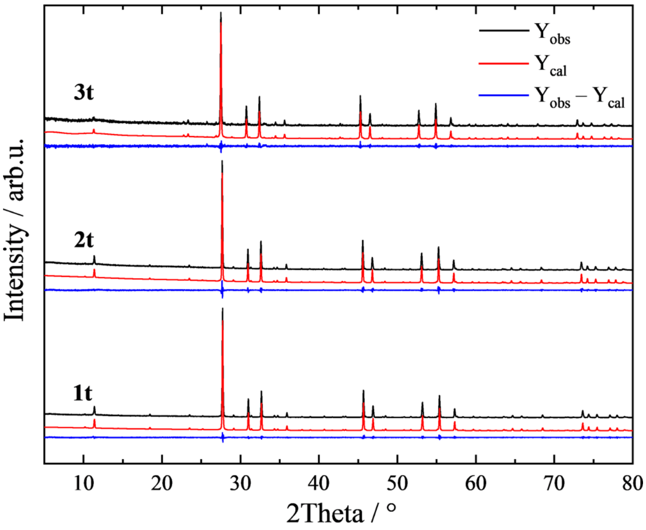

Figure 7. Refined PXRD patterns of $Bi_{14}M^xO_{21+x/2}$ (M = S^{6+} (**1t**), Se^{6+} (**2t**), Re^{7+} (**3t**)) with the space group $I4/m$ based on the crystal structures of tetragonal $Bi_{14}O_{20}(MO_4)$ (M = S,[99] Cr,[100,101] Mo,[101] and W[101]) and $Bi_{14}O_{20}(ReO_{4.5})$.[102]

Table 4. Refined Lattice Parameters of $Bi_{14}M^xO_{21+x/2}$ (M = S^{6+} (1t), Se^{6+} (2t), Re^{7+} (3t)) with the Space Group $I4/m$ Based on the Crystal Structures of Tetragonal $Bi_{14}O_{20}(MO_4)$ (M = S,[99] Cr,[100,101] Mo,[101] and W[101]) and $Bi_{14}O_{20}(ReO_{4.5})$[102]

	1t	2t	3t
r_{Ion} (M)[a]/Å	0.29	0.42	0.53
a/Å	8.64958(5)	8.66779(8)	8.7192(1)
c/Å	17.2685(1)	17.3046(2)	17.4120(3)
V/Å^3	1291.95(2)	1300.11(3)	1323.74(4)
wt % Rietveld	100	100	96.0(10)[b]
d_P/nm	307(3)	383(8)	243(5)
R_{wp}/%	0.073	0.075	0.103
R_{Bragg}	1.178	2.237	1.758

[a] Ionic radius of the dopant "M" (S^{6+}, Se^{6+}, and Re^{7+}) with CN 6.[138]
[b] contains a tiny amount of α-Bi_2O_3 (4.0(10) wt %).

The refined cell parameters of tetragonal $Bi_{14}O_{20}(SO_4)$ (**1t**, a = 8.64958(5) Å, c = 17.2685(1) Å) and $Bi_{14}O_{20}(ReO_{4.5})$ (**3t**, a = 8.7192(1) Å, c = 17.4120(3) Å) are in agreement with the reported values for $Bi_{14}O_{20}(SO_4)$ (a = 8.664(1) Å, c = 17.282(2) Å),[99] and $Bi_{14}O_{20}(ReO_{4.5})$ (a = 8.7216(1) Å, c = 17.4177(2) Å),[102] respectively. The new tetragonal $Bi_{14}O_{20}(SeO_4)$ (**2t**) is isomorphous to the bismuth(III) oxide chalcogenate **1t**. Thus, refinement of the PXRD pattern of **2t** was carried out following the reports by Francesconi et al.,[99] Warda et al.,[100] and Crumpton et al.[101] (Tables S5–S7).

In compound **2t**, the selenium(VI) cations occupy the 4e Wyckoff position, and Se–O bond distances in the range of 2.0(5)–2.3(3) Å are determined, which are slightly larger compared to the typical range of 1.6–1.7 Å.[166,167] The Bi–O distances for Bi(1), Bi(2), and Bi(3) are in the range of d_{Bi1-O} = 2.27(4)–2.8(3) Å, d_{Bi2-O} = 2.07(4)–2.9(4) Å, and d_{Bi3-O} = 2.22(4)–2.67(4) Å, respectively. These values are in the typical range of the Bi–O backbone in $Bi_{14}O_{20}(MO_4)$ (M = Cr,[100,101] Mo,[101] and W[101]) (Table S7).

TG analysis of δ-Bi_2O_3:M (M = S^{6+} (**1c**), Se^{6+} (**2c**), Re^{7+} (**3c**)) reveals a tiny weight loss with $\Delta\omega$ = 0.6–1.4% upon heating to T = 400 °C assigned to the desorption of adsorbed water (Figures S9–S11, Table S8). The mass remains constant upon heating to T = 600 °C. The corresponding DSC curves of **1c** and **2c** reveal signals at T_{Peak} = (471 ± 3) °C with ΔH = −26.22 $kJ \cdot mol^{-1}$ (**1c**, Figure S9) and T_{Peak} = (442 ± 2) °C with ΔH = −7.76 $kJ \cdot mol^{-1}$ (**2c**, Figure S10), which are assigned to the exothermic phase transition from the cubic to the corresponding tetragonal phase of $Bi_{14}O_{20}(MO_4)$ (M = S and Se, respectively). The DSC curve of **3c** shows only a broad signal at T_{Peak} = (737 ± 4) °C with ΔH = 95.44 $kJ \cdot mol^{-1}$, which is assigned to melting (Figure S11). The residues **3t** and **3t′**, obtained after calcination of **3c** at T = 700 °C and the TG/DSC experiment up to T = 800 °C, contain the tetragonal modification of $Bi_{14}O_{20}(ReO_{4.5})$ verified by PXRD studies (Figure S12). It is assumed that ΔH for the phase transition from cubic to tetragonal $Bi_{14}O_{20}(ReO_{4.5})$ is quite low and thus not detected in the DSC experiment.

For the selenium-containing compound **2c**, a rapid weight loss appears at $T \approx$ 700 °C, which is assigned to the loss of

SeO_3 (Figure S10).[168] The broad signal in the DSC curve at T_{Peak} = (776 ± 1) °C is assigned to both the loss of SeO_3 and the phase transition of the bismuth(III) oxide into the HT δ-phase. Upon cooling, a signal appears at T_{Peak} = (630 ± 6) °C, which is indicative of the exothermic crystallization of γ-Bi_2O_3 as it was demonstrated in a former study (Figure S10).[169] The formation of γ-Bi_2O_3 (**BiO-a**) is confirmed by the PXRD pattern of the resulting residue after the TG/DSC experiment (Figure S13). The metastability of the as-obtained γ-Bi_2O_3 (**BiO-a**) is verified by the phase transition into α-Bi_2O_3 (**BiO-b**) after calcination of the selenium-free residue **BiO-a** at T = 600 °C (t = 60 min) on a silver sheet (Figure S13). The thermal behavior of **BiO-a** is in line with our previous studies on the metastability of γ-Bi_2O_3.[170]

Exemplarily for the phase transition from cubic to tetragonal $Bi_{14}M^xO_{21+x/2}$ (M = S^{6+} (**1c**), Se^{6+} (**2c**), Re^{7+} (**3c**)), a HT PXRD experiment was carried out for $Bi_{14}O_{20}(SO_4)$ (**1c**) in the temperature range T = 30−700 °C using a quartz capillary (Figure 8). The reflections of the cubic modification **1c** disappear at T ≈ 450 °C and reflections of the corresponding tetragonal phase appear immediately. At temperatures above T ≈ 490 °C, no further changes are observed, and only reflections of tetragonal $Bi_{14}O_{20}(SO_4)$ are detected. The temperature range for the phase transition from cubic to tetragonal $Bi_{14}O_{20}(SO_4)$ obtained from the HT-PXRD experiment with T = 450−490 °C is in line with the result from the TG/DSC analysis with T = 451−495 °C (Figure S9).

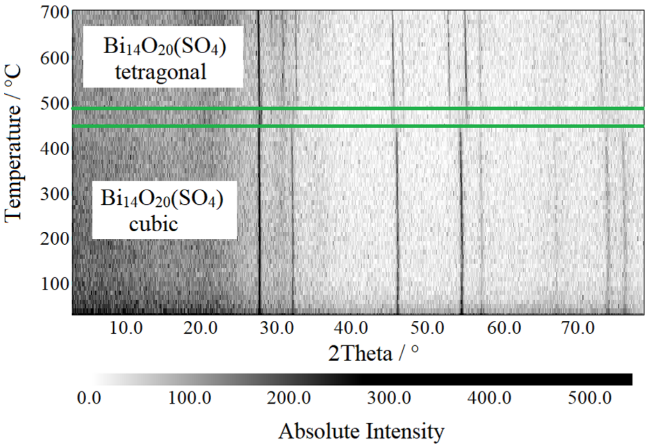

Figure 8. HT-PXRD experiment starting from $Bi_{14}O_{20}(SO_4)$ (**1c**) in a quartz capillary in the temperature range of T = 30−700 °C in air. The phase transition from cubic to tetragonal phase is marked by green bars (T ≈ 450−490 °C).

In addition to the DSC analysis and HT-PXRD experiment, Raman spectra were recorded during heating of cubic $Bi_{14}O_{20}(SO_4)$ (**1c**) from T = 30 °C to T = 600 °C followed by subsequent cooling to T = 25 °C (Figure 9).

The Raman spectrum of cubic $Bi_{14}O_{20}(SO_4)$ (**1c**) does immediately change at temperatures above T = 460 °C, and the broad Bi−O modes below 200 cm^{-1} become significantly sharper. The position of the $\nu_1(SO_4^{2-})$ mode at ν ≈ 964 cm^{-1} strongly depends on the temperature during heating and cooling (Figure 10). The shift to lower wavenumbers upon heating to T = 450 °C is assigned to temperature effects, whereas a slightly stronger shift occurs in the temperature range T = 460−490 °C. This change is caused by the cubic-to-tetragonal phase transition of $Bi_{14}O_{20}(SO_4)$. The shift of the $\nu_1(SO_4^{2-})$ mode upon further heating to T = 600 °C is again assigned to temperature effects. After cooling the tetragonal $Bi_{14}O_{20}(SO_4)$ to T = 25 °C, the $\nu_1(SO_4^{2-})$ mode is located at approx. 956 cm^{-1}.[148,149] The shift of the $\nu_1(SO_4^{2-})$ mode from 964 cm^{-1} in cubic $Bi_{14}O_{20}(SO_4)$ to 956 cm^{-1} in the tetragonal phase demonstrates the structural changes caused by the exothermic phase transition.

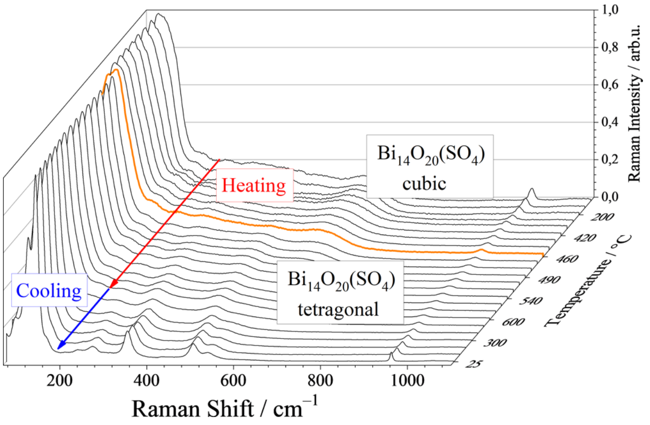

Figure 9. Raman spectra (recorded with a green laser, λ = 514.7 nm) of $Bi_{14}O_{20}(SO_4)$ (**1c**) placed on a SiO_2 slide in the temperature range of T = 25−600 °C in air followed by subsequent cooling to T = 25 °C. The "cubic-to-tetragonal" phase transition is highlighted by an orange line (T = 460 °C).

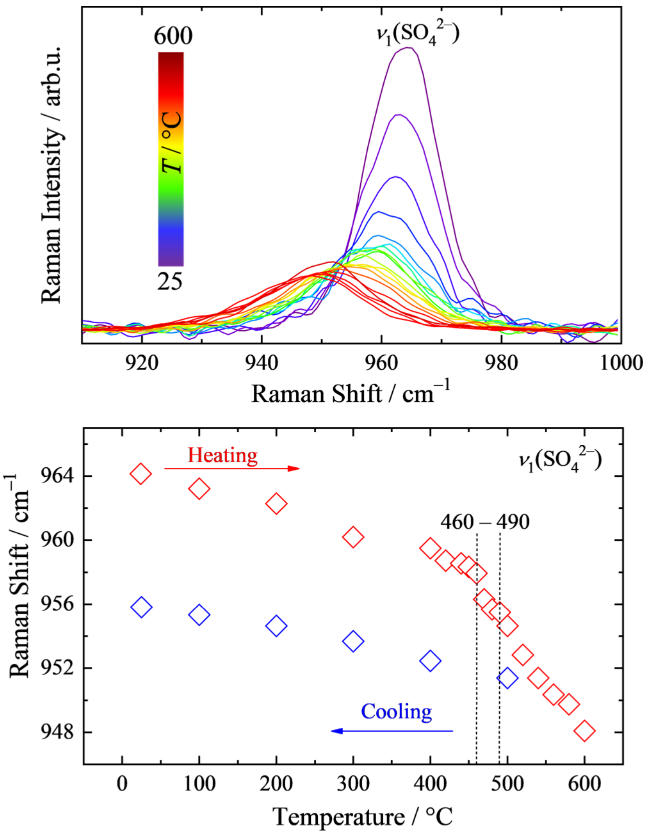

Figure 10. *Top*: Raman shift of the sulfate group (ν_1) in $Bi_{14}O_{20}(SO_4)$ (**1c**) upon heating to T = 600 °C. *Bottom*: Temperature dependence of the $\nu_1(SO_4^{2-})$ Raman shift.

The $\nu_1(SeO_4^{2-})$ mode in $Bi_{14}O_{20}(SeO_4)$ (**2c**) at ν ≈ 814 cm^{-1} shows a similar behavior during heating and cooling procedures in the temperature range T = 25−600 °C (Figure

S14). In addition to the shift of the $\nu_1(SeO_4^{2-})$ mode by temperature effects, a significant stronger shift occurs in the temperature range T = 440−470 °C, which is assigned to the structural changes induced by the cubic-to-tetragonal phase transition. The findings from temperature-dependent Raman studies on compound **2c** match those from the DSC analysis discussed above (Figure S10). After the HT-Raman experiment, the ν_1 mode of the $[SeO_4]^{2-}$ group in tetragonal $Bi_{14}O_{20}(SeO_4)$ is located at $\nu \approx 811$ cm^{-1}.[140,150−153]

As mentioned above, the Bi−O lattice of tetragonal $Bi_{14}M^xO_{21+x/2}$ (M = S^{6+} (**1t**), Se^{6+} (**2t**), Re^{7+} (**3t**)) consists of the coordination polyhedra $[Bi(1)O_{10}]$, $[Bi(2)O_5]$ (distorted tetragonal pyramid), and $[Bi(3)O_8]$ (Figure 1). The corresponding Raman spectra show several Bi−O vibrations in the range of ν = 60−700 cm^{-1} (Figure 11). The evaluation approach reported by Hardcastle et al. dealt with empirical relations between Bi−O bond lengths, bond strengths, and Raman stretching frequencies "ν" of ideal and symmetric Bi−O coordination polyhedra (with Bi−O bond distance "d_{Bi-O}," values given in Å).[147] The least-squares exponential fit given by eq 5 represents the relation between crystallographically determined Bi−O bond lengths and Raman stretching frequencies:[147]

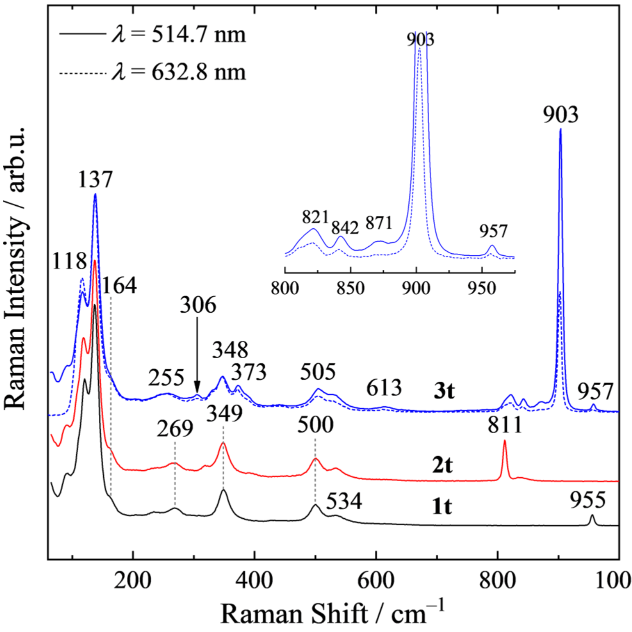

Figure 11. Raman spectra of tetragonal $Bi_{14}M^xO_{21+x/2}$ (M = S^{6+} (**1t**), Se^{6+} (**2t**), Re^{7+} (**3t**)).

$$\nu = 92760 \cdot \exp(-2.511 \cdot d_{Bi-O}) \quad (5)$$

Based on the crystal structures of tetragonal $Bi_{14}O_{20}(SO_4)$,[99] $Bi_{14}O_{20}(SeO_4)$, and $Bi_{14}O_{20}(ReO_{4.5})$,[102] ideal and symmetric vibrations of $[Bi(1)O_{10}]$, $[Bi(2)O_5]$, and $[Bi(3)O_8]$ are expected to be located at ν(Bi1−O) ≈ (91, 120, 234, 300, 330) cm^{-1}, ν(Bi2−O) ≈ (91, 138, 164, 204, 348, 390, 500, 533) cm^{-1}, and ν(Bi3−O) ≈ (91, 118, 266, 300, 330) cm^{-1} (Table S9). Thus, the crystallographically determined Bi−O bond lengths of the Bi−O coordination polyhedra match with the observed Raman stretching frequencies of $Bi_{14}M^xO_{21+x/2}$ (M = S^{6+} (**1t**), Se^{6+} (**2t**), Re^{7+} (**3t**)). The typical ν_1 modes of the sulfate[148,149] and selenate[140] group in **1t** and **2t** are located at 955 and 811 cm^{-1}, respectively. The $[ReO_4]^-$group in **3t** shows vibration bands at 957 cm^{-1} (ν_1), 903 cm^{-1} (ν_3 B_g), 871 cm^{-1} (ν_3 E_g), and 373 cm^{-1} (ν_4).[142,154,155] The vibration bands of the $[ReO_6]^{5-}$ group are located at 821 and 842 cm^{-1} for the ν_1 mode; this splitting is suggested to be the result of a slight distortion of the octahedra. Further vibration bands at 613 cm^{-1} (ν_3) and 306 cm^{-1} (ν_6) are indicative of the $[ReO_6]^{5-}$ group (Figure 11).[142,157]

In the corresponding IR spectrum of compound **3t**, the ν_1 mode $[ReO_6]^{5-}$ shows split vibration bands located at 808 and 841 cm^{-1} (Figure S15), and the ν_3 mode of the $[ReO_4]^-$ group is located at 901 cm^{-1}.

The UV−vis spectrum (Kubelka−Munk function[128,129]) of **3t** shows a broad absorption band with an absorption edge located at λ = (530 ± 2) nm indicating the excitation of **3t** by visible-light absorption (Figure 12).

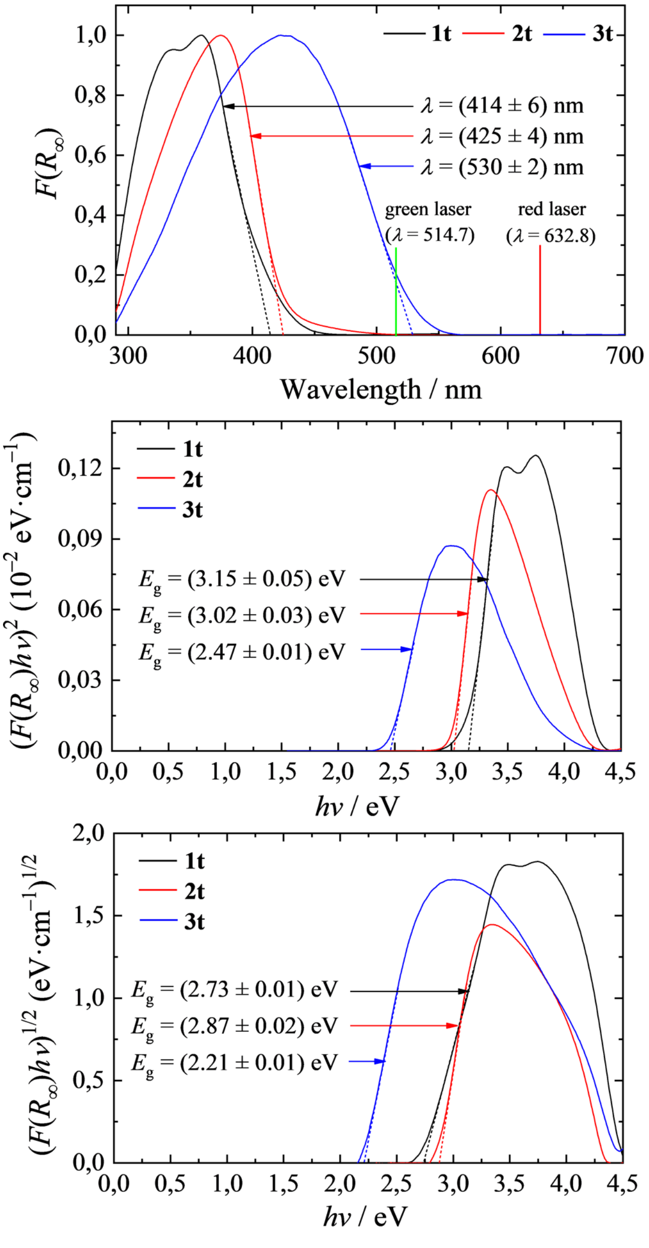

Figure 12. UV−vis absorption spectra (Kubelka−Munk function,[128,129] *top*) and Tauc plots[123,124,130] for the determination of the direct (*middle*) and indirect band-gap energy E_g (*bottom*) of the as-prepared $Bi_{14}M^xO_{21+x/2}$ (M = S^{6+} (**1t**), Se^{6+} (**2t**), Re^{7+} (**3t**)).

Thus, illumination of **3t** with the green laser (λ = 514.7 nm) results in similarly increased Raman signals of the $[ReO_4]^-$ group because of the *Resonance Raman Effect* as discussed above for the cubic phase **3c**.[158−160] Recording the Raman spectrum of **3t** using a green laser causes a significant increase of intensity of the $\nu_3[ReO_4]^-$ mode at 903 cm^{-1} in comparison to the Raman spectrum recorded with a red laser (λ = 632.8 nm, Figure 11). The tetragonal bismuth(III) oxide chalcogenates **1t** and **2t** absorb in the UV region of the light spectrum and exhibit absorption edges at $\lambda \approx 420$ nm. Thus, resonant Raman spectroscopy is hindered for **1t** and **2t** when using a laser with wavelength in the visible-light region. The correlation between visible-light excitation and increased Raman signal is obtained for both the cubic phase **3c** and the tetragonal modification **3t** of $Bi_{14}O_{20}(ReO_{4.5})$. It is concluded that both phases are visible-light-driven semiconductors, whereas $Bi_{14}O_{20}(MO_4)$ (M = S (**1t**), Se (**2t**)) absorb only UV light. The evaluation of the Tauc plots of tetragonal $Bi_{14}M^xO_{21+x/2}$ (M = S^{6+} (**1t**), Se^{6+} (**2t**)) provides band-gap energies of approx. 3 and 2.8 eV for direct and indirect allowed electronic transitions, respectively (Figure 12). For direct and indirect allowed electronic transitions in compound **3t**, corresponding band-gap energies of E_g = (2.47 ± 0.01) and (2.21 ± 0.01) eV are determined from the Tauc plots. Thus, excitation of **3t** using a green laser seems to be likely for both transitions, impeding a final conclusion of **3t** to be a direct or indirect semiconductor.

The TG/DSC analysis of $Bi_{12.25}O_{16.625}(SeO_3)_{1.75}$ (**4c**) up to T = 800 °C demonstrates the sensitivity to oxygen during heating followed by thermal decomposition resulting in the loss of SeO_3 (Figure S16). Upon heating to T = 300 °C, desorption of adsorbed water and partial oxidation of Se^{4+} to Se^{6+} occur for $[Bi_{12.25}O_{16.625}(SeO_3)_{1.75}]\cdot 2.14H_2O_{(ads)}$ (**I**) to become $Bi_{12.25}O_{16.625}(SeO_3)_{1.16}(SeO_4)_{0.59}$ (**II**, Table S10). Complete oxidation of **II** to give $Bi_{12.25}O_{16.625}(SeO_4)_{1.75}$ (**III**) starts at T_{On} = (341 ± 4) °C and is completed at $T \approx 532$ °C ($\Delta H = -79.33$ kJ·mol^{-1}); the increased weight by approx. $\Delta\omega$ = 0.60% corresponds to the required amount of oxygen (0.58 O_2, $\Delta\omega$ = 0.60%) for the oxidation of Se^{4+} to Se^{6+}. The mass remains constant in the temperature range T = 520−650 °C, and the DSC signal at T_{Peak} = (632 ± 3) °C ($\Delta H = -7.11$ kJ·mol^{-1}) is assigned to an exothermic phase transition similar to the cubic-to-tetragonal phase transition process starting from the bismuth(III) oxide chalcogenates **1c** and **2c**. Heating of $Bi_{12.25}O_{16.625}(SeO_4)_{1.75}$ (**III**) to temperatures higher than approx. 650 °C results in the complete loss of the incorporated selenium(VI) oxide (−1.75 SeO_3, Table S10), and the obtained residue consists of bismuth(III) oxide (**IV**, Table S10). The broad signal in the DSC curve at T_{Peak} = (752 ± 3) °C is assigned to both the loss of SeO_3 and the phase transition of the bismuth(III) oxide into the high-temperature δ-phase similar to compound **2c**. During cooling, the DSC curve shows a signal at T_{Peak} = (640 ± 1) °C with $\Delta H = -21.50$ kJ·mol^{-1} in accordance with the exothermic phase transition from δ- into γ-Bi_2O_3 (Figure S16). After the TG/DSC analysis of **4c**, the PXRD pattern of the as-obtained residue confirms the crystallization of γ-Bi_2O_3 (**BiO-c**, Figure S17). Similar to the thermal behavior of γ-Bi_2O_3 (**BiO-a**), the as-obtained γ-Bi_2O_3 (**BiO-c**) is transformed into monoclinic α-Bi_2O_3 (**BiO-d**) after calcination at T = 600 °C on a silver sheet (Figure S17). The TG curve of compound **5c** shows a weight loss upon heating to T = 200 °C, which is assigned to the desorption of adsorbed water ($\Delta\omega$ = 0.46%) from $[Bi_{10.51}O_{14.765}(SO_3)_{0.49}\ (SO_4)_{0.51}]\cdot 0.65H_2O_{(ads)}$ (**I**) to give $Bi_{10.51}O_{14.765}(SO_3)_{0.49}(SO_4)_{0.51}$ (**II**) (Figure S18, Table S11). Upon heating to T = 400 °C, the difference $\Delta\omega$ = 0.31% is assigned to the complete oxidation of S^{4+} (0.49 SO_2 + 0.245 O_2 → 0.49 SO_3; $\Delta\omega$ = 0.31%) to the bismuth(III) oxide sulfate $Bi_{10.51}O_{14.765}(SO_4)$ (**III**). The mass remains constant upon heating to T = 800 °C and during the subsequent cooling. The exothermic oxidation process of S^{4+} to S^{6+} is assigned to the broad signal in the DSC curve starting at T_{On} = (188 ± 1) °C ($\Delta H = -318.87$ kJ·mol^{-1}), which is finished at $T \approx 400$ °C. The crystallization of tetragonal $Bi_{14}O_{20}(SO_4)$ is assigned to the DSC signal at T_{Peak} = (619 ± 4) °C ($\Delta H = -9.01$ kJ·mol^{-1}).

Calcination of **5c** at T = 800 °C results in the formation of bismuth(III) oxide sulfate **5t** containing a mixture of $Bi_8O_{11}(SO_4)$ (**5t-a**, 58.1(10) %) and $Bi_{14}O_{20}(SO_4)$ (**5t-b**, 41.9(10) %,) with tetragonal unit cells based on the refined PXRD pattern using Rietveld methods (Figure S19, Tables S12−S14). The corresponding IR spectrum shows the ν_3-, ν_1-, and ν_4- vibrations of the sulfate group in **5t** located at 1040 cm^{-1} (shoulder at 1110 cm^{-1}), 964 cm^{-1}, and 589 cm^{-1}, respectively (Figure S20).[145] $Bi_8O_{11}(SO_4)$ was first obtained by Crumpton and Greaves after the solid-state reaction of bismuth(III) oxide and $(NH_4)_2SO_4$ at T = 800 °C.[116] The tetragonal phase of $Bi_8O_{11}(SO_4)$ crystallizes in the space group $P4_12_12$, and its superstructure is based on a defective *fluorite*-type subcell (δ-Bi_2O_3).[116] The refined cell parameters of $Bi_8O_{11}(SO_4)$ (**5t-a**) with a = 11.7006(5) Å and c = 22.6217(12) Å are in accordance with those of $Bi_8O_{11}(SO_4)$ reported by Crumpton and Greaves.[116] The crystallization of tetragonal $Bi_8O_{11}(SO_4)$ is assigned to the DSC signal at T_{Peak} = (719 ± 12) °C ($\Delta H = -12.22$ kJ·mol^{-1}, Figure S18) upon cooling. The crystallization of tetragonal $Bi_{14}O_{20}(SO_4)$ (**5t-b**) leads to the DSC signal in the temperature range T = 579−640 °C ($\Delta H = -9.01$ kJ·mol^{-1}, Figure S17) during heating.

In the Raman spectrum of **5t** (Figure 13), the following vibration bands are assigned to the bismuth−oxygen coordination polyhedra of tetragonal $Bi_{14}O_{20}(SO_4)$ (**5t-b**) $[Bi(1)O_{10}]$, ν = 349 cm^{-1}; $[Bi(2)O_5]$, ν = 138 cm^{-1}, 204 cm^{-1}, 501 cm^{-1}, 537 cm^{-1}, and $[Bi(3)O_8]$, ν = 121 cm^{-1}, 275 cm^{-1} similar to $Bi_{14}O_{20}(SO_4)$ (**1t**, Figure 11).[147] Because of the similar bismuth−oxygen bond distances in $Bi_8O_{11}(SO_4)$ (**5t-a**)

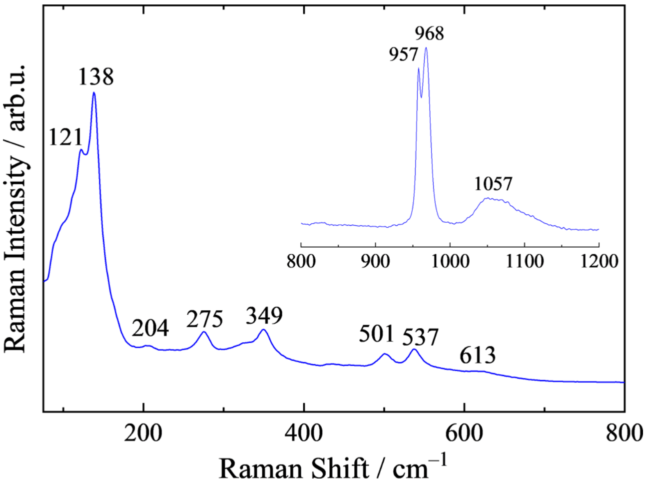

Figure 13. Raman spectrum (recorded with a green laser, λ = 514.7 nm) of $Bi_8O_{11}(SO_4)/Bi_{14}O_{20}(SO_4)$ (**5t**, 58:42) including the range from ν = 800 to 1200 cm^{-1}.

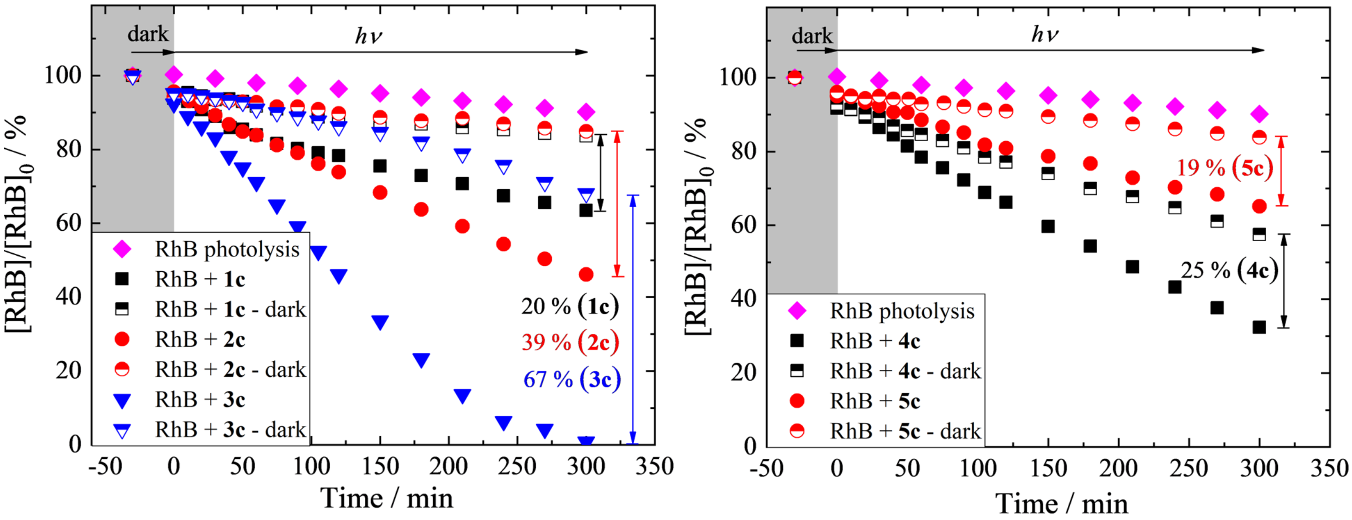

Figure 14. Degradation of RhB under visible-light irradiation (420 nm $\leq \lambda \leq$ 700 nm) in the presence of δ-Bi_2O_3:M (β = 1.0 g·L^{-1}; *left*: M = S^{6+} (**1c**), Se^{6+} (**2c**), and Re^{7+} (**3c**); *right*: M = Se^{4+} (**4c**) and $S^{4+/6+}$ (**5c**)).

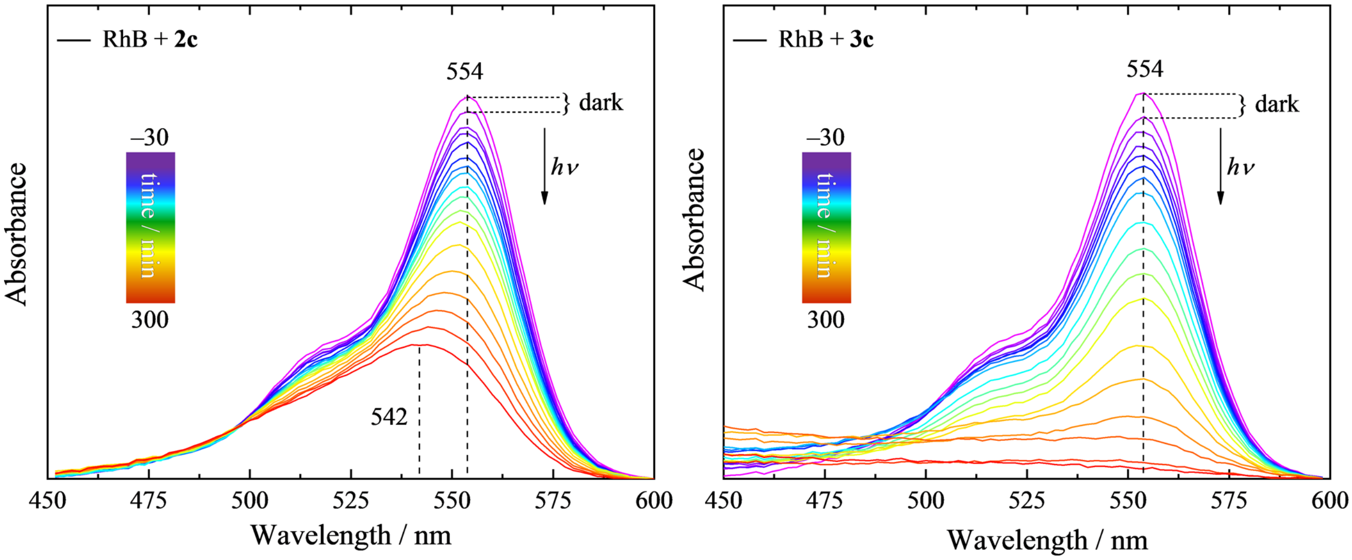

Figure 15. UV–vis spectra of aqueous RhB under visible-light irradiation (420 nm $\leq \lambda \leq$ 700 nm) in the presence of $Bi_{14}O_{20}(SeO_4)$ (**2c**, *left*) and $Bi_{14}O_{20}(ReO_{4.5})$ (**3c**, *right*).

and $Bi_{14}O_{20}(SO_4)$ (**5t-b**), it is difficult to distinguish the Raman bands in the range of 60–700 cm^{-1} between the different bismuth–oxygen frameworks (Figure 13).

Usually, Bi–O bond distances exhibit values >2 Å, but some bonds in tetragonal $Bi_8O_{11}(SO_4)$ are slightly shorter.[116] Crumpton and Greaves assigned this problem to the structural incompleteness of the suggested model, which does not fully consider the coordination of oxygen atoms around the sulfur atoms, thus representing an average structure of the bismuth–oxygen framework.[116] The ν_1 Raman mode of the sulfate group in tetragonal $Bi_{14}O_{20}(SO_4)$ (**5t-b**) is assigned to the vibration band at ν = 957 cm^{-1} in accordance with the ν_1 mode in **1t** (955 cm^{-1}, Figure 11); thus the vibration band of the ν_1 mode of the sulfate group in $Bi_8O_{11}(SO_4)$ (**5t-a**) is located at ν = 968 cm^{-1}.[148,149] The broad vibration band at $\nu \approx$ 1057 cm^{-1} is assigned to the ν_3 mode of the sulfate group in both bismuth(III) oxide sulfates.[148,149] The presence of two $\nu_1(SO_4{}^{2-})$ vibration bands confirms the formation of two different bismuth(III) oxide sulfates in **5t** after calcination of compound **5c** at T = 800 °C.

3.3. Photoinduced Decomposition of RhB in the Presence of δ-Bi_2O_3:M (M = S, Se, and Re).

The photocatalytic conversion of aqueous RhB solution in the presence of the as-prepared samples of δ-Bi_2O_3:M (M = S, Se, and Re; **1c**–**5c**) was carried out under visible-light irradiation (Figure S21). RhB was chosen because it is still used in the paper industry despite its potential to cause mutagenic effects and thus represents an important water contaminant.[171,172] Second, the dye represents a well-suited model compound for photocatalytic decomposition experiments to purify waste water because of its high stability under light irradiation in the absence of a photocatalyst.[173−175]

Compounds **1c**–**5c** (β = 1.0 g·L^{-1}) were dispersed in aqueous RhB solution (c = 10 μM) and stirred in the dark for t = 30 min followed by visible-light illumination (420 nm < λ < 700 nm) for t = 300 min or stirring in the dark (Figure 14). After stirring the suspensions for t = 30 min in the dark, 4–8%

of the initial RhB concentration was decreased by adsorption of the dye molecules on the particle surface of the compounds **1c**−**5c** (Table S15). When visible-light illumination started, a progressive decrease of the RhB concentration was observed for all tested compounds, which is indicative of the photoinduced decomposition of the dye. The UV−vis spectra, which show the decolorization of the RhB solution, are exemplarily given for $Bi_{14}O_{20}(SeO_4)$ (**2c**) and $Bi_{14}O_{20}(ReO_{4.5})$ (**3c**, Figure 15). Without illumination, approx. 15−43% of the dye was adsorbed on the particle surface of **1c**−**5c**. Considering the adsorbed amount of RhB in the dark, the photoinduced conversion of the dye after illumination for t = 300 min in the presence of **1c**−**5c** is in the range of 19−67%. Under the assumption of a first-order decomposition rate law, the reaction rate constants for the conversion of RhB in the presence of compound **1c**, **2c**, **4c**, and **5c** are in the range k = 0.001−0.005 min^{-1}; compound **3c** exhibits the highest value with k = 0.03 min^{-1} (Figure S22, Table S15). The highest decrease in intensity of the RhB absorption band was obtained in the presence of the bismuth(III) oxide perrhenate **3c** (67%) followed by the selenium-containing bismuth(III) oxides **2c** (39%) and **4c** (25%); sulfur-containing bismuth(III) oxides **1c** (S^{6+}, 20%) and **5c** ($S^{4+/6+}$, 19%) show the lowest decrease in intensity of the RhB absorption band. Excitation of the sulfur and selenium containing bismuth(III) oxides **1c**, **2c**, **4c**, and **5c** by visible-light irradiation is not possible because of their large band-gap energies of approx. 3 eV, whereas compound **3c** is a visible-light-driven semiconductor as it was concluded based on the results from UV−vis and Raman spectroscopy. Thus, under the present conditions, bismuth(III) oxides containing sulfur and selenium oxide are low efficient photocatalysts regarding the photoinduced decomposition of aqueous RhB under visible-light irradiation. In comparison to the compounds **1c**, **2c**, **4c**, and **5c**—absorbing solely UV light—the visible-light-driven bismuth(III) oxide perrhenate **3c** shows the highest RhB conversion resulting in the almost complete decolorization of the initial dye solution.

The corresponding UV−vis spectra of aqueous RhB under visible-light irradiation in the presence of $Bi_{14}O_{20}(ReO_{4.5})$ (**3c**) show a rapid decrease of the dye absorption band without any shift of the absorption maximum λ_{max} located at 554 nm, which is indicative of the direct oxidation of the chromophoric system by photogenerated active species via the photocatalytic process.[176,177] In the presence of $Bi_{14}O_{20}(SeO_4)$ (**2c**), a significant blue shift of λ_{max} to approx. 542 nm occurred (Figure 15), which is indicative of the ongoing *N*-deethylation process of RhB to give *N*,*N*,*N*'-triethylrhodamine (λ_{max} = 539 nm) via the photosensitive mechanism.[178,179] In the photoinduced decomposition of RhB, the photocatalytic and the photosensitive mechanism are independent and competing processes.[180] The photocatalytic mechanism requires the excitation of the semiconductor by light absorption to generate charge carriers such as electrons (e^-) and holes (h^+) in the CB and VB, respectively.[180,181] The photosensitive mechanism is based on the excitation of the dye molecule by light absorption into its singlet state.[178-180] However, the formation of the rhodamine B radical cation ($RhB^{\bullet+}$) as a key species via electron transfer from the dye molecule to the semiconductor is essential for both mechanisms and adsorbed oxygen acts as an electron scavenger.[178-180,182] The subsequent decomposition of the conjugated π-system by the photocatalytic mechanism can be traced by the continuously decreasing intensity of the dye absorption band in the UV−vis spectrum in aqueous solution without any shift of the absorption maximum (λ_{max} = 555 nm) as it was demonstrated in the presence of $Bi_{14}O_{20}(ReO_{4.5})$ (**3c**).[179,182] The stepwise *N*-deethylation of RhB via the photosensitive mechanism gives intermediates with characteristic absorption maxima in aqueous solution such as *N*,*N*,*N*'-triethylrhodamine (λ_{max} = 539 nm), *N*,*N*'-diethylrhodamine (λ_{max} = 522 nm), *N*-ethylrhodamine (λ_{max} = 510 nm), and rhodamine (λ_{max} = 498 nm).[178,179] Thus, the *N*-deethylation of RhB can be traced by this significant blue shift of the absorption maximum of the dye absorption band in the UV−vis spectrum in aqueous solution as it was shown in the presence of $Bi_{14}O_{20}(SeO_4)$ (**2c**).[178,179,182,183]

The UV−vis spectra of aqueous RhB in the presence of compounds **1c**, **4c**, and **5c** show an ongoing decrease in intensity and only a small blue shift of the absorption maximum (λ_{max} = 554 nm) to approx. 552 nm, which is indicative of the photosensitive mechanism (Figures S23 and S24). Thus, the photosensitive mechanism exhibits a higher contribution for the large-band-gap semiconductors **1c**, **2c**, **4c**, and **5c**, whereas photoinduced decomposition of RhB mainly follows the photocatalytic process in the presence of compound **3c** as it was demonstrated by UV−vis spectroscopy (Figures 15, S23, and S24).

After dispersing δ-Bi_2O_3:M (M = S, Se, and Re; **1c**−**5c**) under visible-light irradiation and in the dark, the PXRD patterns of compounds **1c**−**3c** show low-intensity reflections of $Bi_2O_2CO_3$ in addition to the *fluorite*-type δ-Bi_2O_3:M (M = S, Se, and Re), whereas only reflections of the initial cubic phase were detected in the corresponding patterns of **4c** and **5c**, respectively (Figure S25). The formation of $Bi_2O_2CO_3$ in the presence of **1c**−**3c** is the result of the so-called photocorrosion, which is a well-known side reaction during photoinduced decomposition of organic pollutants in the presence of bismuth(III) oxide polymorphs as a photocatalyst such as α-,[184,185] β-,[30,186] and γ-Bi_2O_3.[170] It is noteworthy that formation of $Bi_2O_2CO_3$ is also possible by the contact of the bismuth(III)-based oxide with CO_2(aq) or from air.[165] As mentioned before, the resistance of $Bi_{12.25}O_{16.625}(SeO_3)_{1.75}$ (**4c**) and $Bi_{10.51}O_{14.765}(SO_3)_{0.49}(SO_4)_{0.51}$ (**5c**) compared to $Bi_{14}O_{20}(SO_4)$ (**1c**) and $Bi_{14}O_{20}(SeO_4)$ (**2c**) against the reaction with CO_2 to $Bi_2O_2CO_3$ is assigned to the higher content of Se^{4+} and $S^{4+/6+}$ replacing the trivalent bismuth cations in the *fluorite*-type lattice.

To date, "state-of-the-art" photocatalysts used in the photocatalytic decomposition of RhB are typically semiconductors such as UV-light-driven TiO_2,[187−190] ZnO,[191] as well as visible-light-driven g-C_3N_4,[187,189,192] and Bi_2O_3.[52,189,193,194] However, it is challenging to compare the efficiency of the different semiconductors because of the lack of a uniform photocatalysis setup (catalyst loading, dye concentration, particle surface area, and light source; see Table S16). Compared to visible-light-driven photocatalysts such as g-C_3N_4,[187,189] and α-/β-Bi_2O_3,[193] the as-prepared $Bi_{14}O_{20}(ReO_{4.5})$ (**3c**) shows a lower RhB conversion. Under UV irradiation, TiO_2,[190] and ZnO[191] also provide improved RhB conversion compared to compound **3c**. Still, under visible-light illumination, the as-prepared bismuth(III) oxide perrhenate **3c** shows higher efficiency because of its lower band-gap energy (E_g < 3 eV) compared to TiO_2[187] (Table S16).

To provide a more reliable classification of $Bi_{14}O_{20}(ReO_{4.5})$ (**3c**), the obtained results of the photoinduced decomposition experiments of RhB in the presence of visible-light-driven **3c** were compared to other systems using δ-Bi_2O_3 or isostructural compounds as a photocatalyst under similar conditions. Almost complete decolorization of RhB (c = 10 μM) was obtained in the presence of particles of compound **3c** (A_{BET} = 11 $m^2 \cdot g^{-1}$, β = 1.0 $g \cdot L^{-1}$) under visible-light irradiation using a Xe-lamp (420 nm $\leq \lambda \leq$ 700 nm, P = 300 W) for t = 300 min. In the work by Zhou et al., approx. 90% RhB conversion (c = 10 μM) was reported using particles of vanadate-stabilized δ-Bi_2O_3 (β = 1.0 $g \cdot L^{-1}$) with a much higher specific surface area ($A_{BET} \approx$ 70 $m^2 \cdot g^{-1}$) under visible-light irradiation ($\lambda \geq$ 420 nm) for t = 150 min, which was performed using a much more powerful Xe-lamp (P = 500 W).[35] Compared to the conditions reported by Zhou et al., we conclude that $Bi_{14}O_{20}(ReO_{4.5})$ is a more efficient photocatalyst than vanadate-stabilized δ-Bi_2O_3.[35] The vanadate-stabilized δ-Bi_2O_3 reported by Wu et al. provides the complete decolorization of the aqueous RhB solution (c = 10 μM) after illumination for t = 120 min using a white-light T5 lamp (P = 64 W).[34] Despite the five times lower power of the light source, the photocatalyst loading was 15 times higher compared to the loading of compound **3c** in our work; thus we conclude a higher efficiency for compound **3c**.[34] Finally, Zhang et al. demonstrated an almost complete decolorization of RhB (c = 10 μM) in the presence of δ-Bi_2O_3 (β = 0.4 $g \cdot L^{-1}$) under visible-light irradiation for t = 120 min using a powerful Xe-lamp (P = 500 W).[27] This system is concluded to be equally efficient compared to the efficiency of $Bi_{14}O_{20}(ReO_{4.5})$ (**3c**) under visible-light irradiation in the present work.

4. CONCLUSIONS

Herein, we demonstrate in detail the synthesis and characterization of metastable δ-Bi_2O_3:M (M = S, Se, and Re) with an oxygen-defective *fluorite*-type crystal structure obtained from alkaline coprecipitation of the bismuth oxido cluster $[Bi_{38}O_{45}(OMc)_{24}(dmso)_9] \cdot 2dmso \cdot 7H_2O$ (**A**) in the presence of appropriate sulfur-, selenium-, or rhenium-containing additives followed by thermal treatment of the reaction mixture in a microwave reactor. The as-prepared cubic compounds ($Fm\bar{3}m$) exhibit the formulas $Bi_{14}O_{20}(SO_4)$ (**1c**), $Bi_{14}O_{20}(SeO_4)$ (**2c**), $Bi_{14}O_{20}(ReO_{4.5})$ (**3c**), $Bi_{12.25}O_{16.625}(SeO_3)_{1.75}$ (**4c**), and $Bi_{10.51}O_{14.765}(SO_3)_{0.49}(SO_4)_{0.51}$ (**5c**), where **2c**, **4c**, and **5c** represent new nonmetal containing bismuth(III) oxides. Thus, the microwave-assisted coprecipitation approach is a well-suited method to provide access to novel metastable compounds in bismuth(III)-based chemistry. Calcination of **1c**−**3c** results in a phase transition to give the corresponding tetragonal modifications $Bi_{14}O_{20}(SO_4)$ (**1t**), $Bi_{14}O_{20}(SeO_4)$ (**2t**), and $Bi_{14}O_{20}(ReO_{4.5})$ (**3t**) with the space group $I4/m$. Calcination of selenium-containing bismuth(III) oxides results in the complete loss of SeO_3 (after previous oxidation of Se^{4+} in **4c**), whereas sulfur- and rhenium-containing compounds **1c**, **3c**, and **5c** are thermally stable. The results obtained from UV−vis and Raman spectroscopy revealed that both the cubic (**3c**) and tetragonal (**3t**) modifications of $Bi_{14}O_{20}(ReO_{4.5})$ are visible-light-driven semiconductors (E_g < 3 eV), whereas sulfur- and selenium-containing bismuth(III) oxides are limited to the UV-light region (E_g > 3 eV). Thus, only the rhenium-containing compound **3c** enables the photocatalytic decomposition of RhB by direct excitation of the semiconductor by visible-light illumination. The cubic compounds **1c**, **2c**, **4c**, and **5c** show low RhB conversions and blue shifted absorption bands of the dye are the result of the photosensitive mechanism. Photocorrosion (reaction of Bi_2O_3-based semiconductors with CO_2 to give $Bi_2O_2CO_3$) occurred after the RhB decomposition experiment under visible-light irradiation and also in the dark for **1c**−**3c**. Compounds **4c** and **5c** resist the photocorrosion process presumably because of the higher dopant content. Thus, high conversion in the photoinduced decomposition of RhB under visible-light irradiation such as in the presence of compound **3c** is coupled with ongoing consumption of the photocatalyst, whereas compounds **4c** and **5c** still retain their composition but provide only moderate RhB conversions.

■ ASSOCIATED CONTENT

Supporting Information

The Supporting Information is available free of charge at https://pubs.acs.org/doi/10.1021/acs.inorgchem.1c03330.

> PXRD patterns, EDX spectra, DLS data, IR and Raman spectra, TG/DSC analyses, and details of the photocatalytic decomposition experiments (PDF)

■ AUTHOR INFORMATION

Corresponding Author

Michael Mehring − *Fakultät für Naturwissenschaften, Institut für Chemie, Professur Koordinationschemie, Technische Universität Chemnitz, Chemnitz 09107, Germany; Center for Materials, Architectures and Integration of Nanomembranes (MAIN), Technische Universität Chemnitz, Chemnitz 09107, Germany;* orcid.org/0000-0001-6485-6156; Email: michael.mehring@chemie.tu-chemnitz.de

Authors

Marcus Weber − *Fakultät für Naturwissenschaften, Institut für Chemie, Professur Koordinationschemie, Technische Universität Chemnitz, Chemnitz 09107, Germany; Center for Materials, Architectures and Integration of Nanomembranes (MAIN), Technische Universität Chemnitz, Chemnitz 09107, Germany*

Raul D. Rodriguez − *Fakultät für Naturwissenschaften, Institut für Physik, Professur Halbleiterphysik, Technische Universität Chemnitz, Chemnitz 09107, Germany; Tomsk Polytechnic University, 634034 Tomsk, Russia;* orcid.org/0000-0003-4016-1469

Dietrich R.T. Zahn − *Center for Materials, Architectures and Integration of Nanomembranes (MAIN), Technische Universität Chemnitz, Chemnitz 09107, Germany; Fakultät für Naturwissenschaften, Institut für Physik, Professur Halbleiterphysik, Technische Universität Chemnitz, Chemnitz 09107, Germany;* orcid.org/0000-0002-8455-4582

Klaus Stöwe − *Fakultät für Naturwissenschaften, Institut für Chemie, Professur Chemische Technologie, Technische Universität Chemnitz, Chemnitz 09107, Germany*

Complete contact information is available at:
https://pubs.acs.org/10.1021/acs.inorgchem.1c03330

Author Contributions

The manuscript was written through contributions of all authors. All authors have given approval to the final version of the manuscript.

Funding

This work has been supported by the Deutsche Forschungsgemeinschaft (DFG SPP1415: Crystalline Nonequilibrium Phases − Preparation, Characterization and in situ Studies of Formation Mechanisms; ME 2284/3-2.)

Notes

The authors declare no competing financial interest.

■ ACKNOWLEDGMENTS

This publication contains parts including revised versions of the schemes, tables, and figures of the PhD thesis "Synthese und Charakterisierung von Bismut(III)-basierten Halbleitern ausgehend von homo- und heterometallischen Bismutoxidoclustern "of Marcus Weber published in 2021 at Technische Universität Chemnitz.[195] We gratefully thank Prof. Stefan Spange and Prof. Michael Sommer for access to the ATR-IR and UV−vis instruments. We thank Birgit Kempe and Dipl. Chem. Sabine Engelmann for CHNS analyses. We would like to thank Dr. Benjamin Büchter and Dr. Benjamin Mielke for performing EDX-analyses and Dipl.-Chem. Julian Noll for performing TG/DSC analyses. We like to thank M. Wachs for recording the Xe-lamp emission spectrum. Raul D. Rodriguez thanks the Tomsk Polytechnic University 5-100 Program.

■ DEDICATION

Dedicated to Prof. Dr. Josef Breu on the Occasion of his 60th Birthday.

■ REFERENCES

(1) Sillén, L. G. X-Ray Studies on Bismuth Trioxide. *Ark. Kem. Mineral. Geol.* **1937**, *12 A*, 1−15.

(2) Schumb, W. C.; Rittner, E. S. Polymorphism of Bismuth Trioxide. *J. Am. Chem. Soc.* **1943**, *65*, 1055−1060.

(3) Gattow, G.; Schröder, H. Über Wismutoxide. III. Die Kristallstruktur der Hochtemperaturmodifikation von Wismut(III)-Oxid (δ-Bi_2O_3). *Z. Anorg. Allg. Chem.* **1962**, *318*, 176−189.

(4) Gualtieri, A. F.; Immovilli, S.; Prudenziati, M. Powder X-ray Diffraction Data for the New Polymorphic Compound ω-Bi_2O_3. *Powder Diffr.* **1997**, *12*, 90−92.

(5) Atou, T.; Faqir, H.; Kikuchi, M.; Chiba, H.; Syono, Y. A New High-Pressure Phase of Bismuth Oxide. *Mater. Res. Bull.* **1998**, *33*, 289−292.

(6) Ghedia, S.; Locherer, T.; Dinnebier, R.; Prasad, D. L. V. K.; Wedig, U.; Jansen, M.; Senyshyn, A. High-Pressure and High-Temperature Multianvil Synthesis of Metastable Polymorphs of Bi_2O_3: Crystal Structure and Electronic Properties. *Phys. Rev. B* **2010**, *82*, No. 024106.

(7) Cornei, N.; Tancret, N.; Abraham, F.; Mentré, O. New ε-Bi_2O_3 Metastable Polymorph. *Inorg. Chem.* **2006**, *45*, 4886−4888.

(8) Ma, J.; Zhang, L. Z.; Wang, Y. H.; Lei, S. L.; Luo, X. B.; Chen, S. H.; Zeng, G. S.; Zou, J. P.; Luo, S. L.; Au, C. T. Mechanism of 2,4-Dinitrophenol Photocatalytic Degradation by ζ-Bi_2O_3/Bi_2MoO_6 Composites under Solar and Visible Light Irradiation. *Chem. Eng. J.* **2014**, *251*, 371−380.

(9) Aidhy, D. S.; Sinnott, S. B.; Wachsman, E. D.; Phillpot, S. R.; Nino, J. C. Structure of δ-Bi_2O_3 from Density Functional Theory: A Systematic Crystallographic Analysis. *J. Solid State Chem.* **2009**, *182*, 1222−1228.

(10) Wachsman, E. D.; Boyapati, S.; Jiang, N. X. Effect of Dopant Polarizability on Oxygen Sublattice Order in Phase-Stabilized Cubic Bismuth Oxides. *Ionics* **2001**, *7*, 1−6.

(11) Sammes, N. M.; Tompsett, G. A.; Näfe, H.; Aldinger, F. Bismuth Based Oxide Electrolytes - Structure and Ionic Conductivity. *J. Eur. Ceram. Soc.* **1999**, *19*, 1801−1826.

(12) Punn, R.; Feteira, A. M.; Sinclair, D. C.; Greaves, C. Enhanced Oxide Ion Conductivity in Stabilized δ-Bi_2O_3. *J. Am. Chem. Soc.* **2006**, *128*, 15386−15387.

(13) Bayliss, R. D.; Cook, S. N.; Kotsantonis, S.; Chater, R. J.; Kilner, J. A. Oxygen Ion Diffusion and Surface Exchange Properties of the α- and δ-Phases of Bi_2O_3. *Adv. Energy Mater.* **2014**, *4*, No. 1301575.

(14) Fedorov, S. V.; Sedov, M. S.; Belousov, V. V. Functionally Graded IT-MOFC Electrolytes Based on Highly Conductive δ-Bi_2O_3−0.2 wt % B_2O_3 Composite with Molten Grain Boundaries. *ACS Appl. Energy Mater.* **2019**, *2*, 6860−6865.

(15) Ahila, M.; Dhanalakshmi, J.; Selvakumari, J. C.; Padiyan, D. P. Heat Treatment Effect on Crystal Structure and Design of Highly Sensitive Room Temperature CO_2 Gas Sensors Using Anodic Bi_2O_3 Nanoporous Formed in a Citric Acid Electrolyte. *Mater. Res. Express* **2016**, *3*, No. 105025.

(16) Cabot, A.; Marsal, A.; Arbiol, J.; Morante, J. R. Bi_2O_3 as a Selective Sensing Material for NO Detection. *Sensors Actuators B Chem.* **2004**, *99*, 74−89.

(17) Park, S.; An, S.; Ko, H.; Jin, C.; Lee, C. Enhanced Gas Sensing Properties of Bi_2O_3-Core/In_2O_3-Shell Nanorod Gas Sensors. *Bull. Korean Chem. Soc.* **2012**, *33*, 3368−3372.

(18) Liu, L.; Chen, N.; Lei, Y.; Xue, X.; Li, L.; Wang, J.; Komarneni, S.; Zhu, H.; Yang, D. J. Micro-Nanostructured δ-Bi_2O_3 with Surface Oxygen Vacancies as Superior Adsorbents for SeO_x^{2-} Ions. *J. Hazard. Mater.* **2018**, *360*, 279−287.

(19) Liu, L.; Liu, W.; Zhao, X.; Chen, D.; Cai, R.; Yang, W.; Komarneni, S.; Yang, D. Selective Capture of Iodide from Solutions by Microrosette-Like δ-Bi_2O_3. *ACS Appl. Mater. Interfaces* **2014**, *6*, 16082−16090.

(20) Shi, M.; Guo, C.; Li, J.; Li, J.; Zhang, L.; Wang, X.; Ju, Y.; Zheng, J.; Li, X. Removal of Bromide from Water by Adsorption on Nanostructured δ-Bi_2O_3. *J. Nanosci. Nanotechnol.* **2017**, *17*, 6951−6956.

(21) Wang, H.; Wang, S.; Zhao, M.; Li, Y.; Kong, F. Removal of Arsenic from Aqueous Solution using Microflower-like δ-Bi2O3 as Adsorbent: Adsorption Characteristics and Mechanisms. *J. Dispers. Sci. Technol.* **2020**, *41*, 2026−2036.

(22) Gong, S.; Han, Q.; Wang, X.; Zhu, J. Controlled Synthesis of Bismuth-Containing Compounds (α-, β- and δ-Bi_2O_3, $Bi_5O_7NO_3$ and $Bi_6O_6(OH)_2(NO_3)_4{\cdot}2H_2O$) and Their Photocatalytic Performance. *CrystEngComm* **2015**, *17*, 9185−9192.

(23) Medina, J. C.; Bizarro, M.; Silva-Bermudez, P.; Giorcelli, M.; Tagliaferro, A.; Rodil, S. E. Photocatalytic Discoloration of Methyl Orange Dye by δ-Bi_2O_3 Thin Films. *Thin Solid Films* **2016**, *612*, 72−81.

(24) Sudrajat, H. Unprecedented Ultrahigh Photocatalytic Activity of δ-Bi_2O_3 for Cylindrospermopsin Decomposition. *J. Nanopart. Res.* **2017**, *19*, 369.

(25) Sudrajat, H.; Sujaridworakun, P. Low-Temperature Synthesis of δ-Bi_2O_3 Hierarchical Nanostructures Composed of Ultrathin Nanosheets for Efficient Photocatalysis. *Mater. Des.* **2017**, *130*, 501−511.

(26) Xie, J. S.; Li, L. S.; Tian, C. A.; Han, C. L.; Zhao, D. F. Template-Free Synthesis of Hierarchical Constructed Flower-Like δ-Bi_2O_3 Microspheres with Photocatalytic Performance. *Micro Nano Lett.* **2012**, *7*, 651−653.

(27) Zhang, J.; Han, Q.; Wang, X.; Zhu, J.; Duan, G. Synthesis of δ-Bi_2O_3 Microflowers and Nanosheets using $CH_3COO(BiO)$ Self-Sacrifice Precursor. *Mater. Lett.* **2016**, *162*, 218−221.

(28) Cheng, H.; Huang, B.; Lu, J.; Wang, Z.; Xu, B.; Qin, X.; Zhang, X.; Dai, Y. Synergistic Effect of Crystal and Electronic Structures on the Visible-Light-Driven Photocatalytic Performances of Bi_2O_3 Polymorphs. *Phys. Chem. Chem. Phys.* **2010**, *12*, 15468−15475.

(29) Schlesinger, M.; Schulze, S.; Hietschold, M.; Mehring, M. Metastable β-Bi_2O_3 Nanoparticles with High Photocatalytic Activity from Polynuclear Bismuth Oxido Clusters. *Dalton Trans.* **2013**, *42*, 1047−1056.

(30) Schlesinger, M.; Weber, M.; Schulze, S.; Hietschold, M.; Mehring, M. Metastable β-Bi_2O_3 Nanoparticles with Potential for Photocatalytic Water Purification Using Visible Light Irradiation. *ChemistryOpen* **2013**, *2*, 146−155.

(31) Kekade, S. S.; Gaikwad, P. V.; Raut, S. A.; Choudhary, R. J.; Mathe, V. L.; Phase, D.; Kshirsagar, A.; Patil, S. I. Electronic Structure of Visible Light-Driven Photocatalyst δ-$Bi_{11}VO_{19}$ Nanoparticles Synthesized by Thermal Plasma. *ACS Omega* **2018**, *3*, 5853−5864.

(32) Lu, Y. T.; Chen, L. Y.; Huang, Y. L.; Cheng, H.; Kim, S. I.; Seo, H. J. Optical Properties and Visible Light-Driven Photocatalytic Activity of $Bi_{11}VO_{19}$ Nanoparticles with δ-Bi_2O_3-Structure. *J. Alloys Compd.* **2015**, *640*, 226−232.

(33) Sudrajat, H. Chemical State and Local Structure of V Species Incorporated in δ-Bi_2O_3 Photocatalysts. *J. Mater. Sci.* **2018**, *53*, 1088−1096.

(34) Wu, Y.-C.; Huang, Y.-T.; Yang, H.-Y. Crystallization Mechanism and Photocatalytic Performance of Vanadium-Modified Bismuth Oxide Through Precipitation Processes at Room Temperature. *CrystEngComm* **2016**, *18*, 6881−6888.

(35) Zhou, L.; Wang, W.; Xu, H.; Sun, S.; Shang, M. Bi_2O_3 Hierarchical Nanostructures: Controllable Synthesis, Growth Mechanism, and Their Application in Photocatalysis. *Chem. − Eur. J.* **2009**, *15*, 1776−1782.

(36) Gao, X.; Shang, Y.; Liu, L.; Fu, F. Multilayer Ultrathin Ag-δ-Bi_2O_3 with Ultrafast Charge Transformation for Enhanced Photocatalytic Nitrogen Fixation. *J. Colloid Interface Sci.* **2019**, *533*, 649−657.

(37) Gao, X.; Shang, Y.; Liu, L.; Gao, K. Ag Plasmon Resonance Promoted 2D AgBr-δ-Bi_2O_3 Nanosheets with Enhanced Photocatalytic Ability. *J. Alloys Compd.* **2019**, *803*, 565−575.

(38) Gao, X.; Shang, Y.; Gao, K.; Fu, F. Plasmon Sensitized Heterojunction 2D Ultrathin Ag/AgI-δ-Bi_2O_3 for Enhanced Photocatalytic Nitrogen Fixation. *Nanomaterials* **2019**, *9*, 781.

(39) Wu, Z.; Zeng, D.; Liu, X.; Yu, C.; Yang, K.; Liu, M. Hierarchical δ-$Bi_2O_3/Bi_2O_2CO_3$ Composite Microspheres: Phase Transformation Fabrication, Characterization and High Photocatalytic Performance. *Res. Chem. Intermed.* **2018**, *44*, 5995−6010.

(40) Yin, Y.; Li, F.; Zhan, Q.; Jiang, D.; Chen, R. Synthesis of δ-Bi_2O_3/Bi_2MoO_6 Composites with Enhanced Photocatalytic Activity by Hydrothermal Method. *Mater. Res. Bull.* **2018**, *103*, 47−54.

(41) Chen, J.; Zhan, J.; Li, Q. Exploration and Crystal Phase Engineering from Bismuthinite Ore to Visible-Light Responsive Photocatalyst of Bi_2O_3. *J. Environ. Chem. Eng.* **2019**, *7*, No. 103375.

(42) Lunca Popa, P.; Sønderby, S.; Kerdsongpanya, S.; Lu, J.; Bonanos, N.; Eklund, P. Highly Oriented δ-Bi_2O_3 Thin Films Stable at Room Temperature Synthesized by Reactive Magnetron Sputtering. *J. Appl. Phys.* **2013**, *113*, No. 046101.

(43) Gomez, C. L.; Depablos-Rivera, O.; Medina, J. C.; Silva-Bermudez, P.; Muhl, S.; Zeinert, A.; Rodil, S. E. Stabilization of the Delta-Phase in Bi_2O_3 Thin Films. *Solid State Ionics* **2014**, *255*, 147−152.

(44) Baqiah, H.; Talib, Z. A.; Liew, J. Y. C.; Shaari, A. H.; Zainal, Z.; Fudzi, L. M. Effects of Precursor Concentration on the Microstructural, Optical and Photoelectrochemical Properties of Bi_2O_3 Films Synthesized by Sol-Gel Method. *Optik* **2020**, *206*, No. 164303.

(45) Gomez, C. L.; Rodil, S. E. High Stability and AC-Conductivity of Cubic Fluorite-Bi_2O_3 Films Synthesized by Magnetron Sputtering. *Solid State Ionics* **2017**, *309*, 100−109.

(46) Jiang, J.; Lim, D. G.; Ramadoss, K.; Ramanathan, S. Ionic Conduction and Unipolar Resistance Switching in δ-phase Bi_2O_3 Thin Films. *Solid-State Electron.* **2018**, *146*, 13−20.

(47) Bohannan, E. W.; Jaynes, C. C.; Shumsky, M. G.; Barton, J. K.; Switzer, J. A. Low-Temperature Electrodeposition of the High-Temperature Cubic Polymorph of Bismuth(III) Oxide. *Solid State Ionics* **2000**, *131*, 97−107.

(48) Huang, C. C.; Leu, I. C.; Fung, K. Z. Fabrication of δ-Bi_2O_3 Nanowires. *Electrochem. Solid-State Lett.* **2005**, *8*, A204−A206.

(49) Harwig, H. A. On the Structure of Bismuthsesquioxide: the α, β, γ and δ-Phase. *Z. Anorg. Allg. Chem.* **1978**, *444*, 151−166.

(50) Wachsman, E. D.; Lee, K. T. Lowering the Temperature of Solid Oxide Fuel Cells. *Science* **2011**, *334*, 935−939.

(51) Sanna, S.; Esposito, V.; Andreasen, J. W.; Hjelm, J.; Zhang, W.; Kasama, T.; Simonsen, S. B.; Christensen, M.; Linderoth, S.; Pryds, N. Enhancement of the Chemical Stability in Confined δ-Bi_2O_3. *Nat. Mater.* **2015**, *14*, 500−504.

(52) Zahid, A. H.; Han, Q. F. A Review on the Preparation, Microstructure, and Photocatalytic Performance of Bi_2O_3 in Polymorphs. *Nanoscale* **2021**, *13*, 17687−17724.

(53) Watanabe, A. Is it Possible to Stabilize δ-Bi_2O_3 by an Oxide Additive? *Solid State Ionics* **1990**, *40-41*, 889−892.

(54) Jiang, N. X.; Wachsman, E. D. Structural Stability and Conductivity of Phase-Stabilized Cubic Bismuth Oxides. *J. Am. Ceram. Soc.* **1999**, *82*, 3057−3064.

(55) Kruidhof, H.; Seshan, K.; Lippens, B. C.; Gellings, P. J.; Burggraaf, A. J. Bismuth Oxide Based Ceramics with Improved Electrical and Mechanical Properties: Part I. Preparation and Characterization. *Mater. Res. Bull.* **1987**, *22*, 1635−1643.

(56) Kruidhof, H.; Seshan, K.; van de Velde, G. M. H.; de Vries, K. J.; Burggraaf, A. J. Bismuth Oxide Based Ceramics with Improved Electrical and Mechanical Properties: Part II. Structural and Mechanical Properties. *Mater. Res. Bull.* **1988**, *23*, 371−377.

(57) Zhereb, V. P.; Kargin, Y. F.; Zhereb, L. A.; Mironova, V. A.; Skorikov, V. M. Stable and Metastable Phase Equilibria in the Bi_2O_3−$BiPO_4$ System. *Inorg. Mater.* **2003**, *39*, 859−862.

(58) Dreyer, J. A. H.; Pokhrel, S.; Birkenstock, J.; Hevia, M. G.; Schowalter, M.; Rosenauer, A.; Urakawa, A.; Teoh, W. Y.; Mädler, L. Decrease of the Required Dopant Concentration for δ-Bi_2O_3 Crystal Stabilization through Thermal Quenching during Single-Step Flame Spray Pyrolysis. *CrystEngComm* **2016**, *18*, 2046−2056.

(59) Najim, A. A. Synthesis and Characterizations of $(\delta\text{-}Bi_2O_3)_{0.93}(TiO_2)_{0.07}$ Thin Films Grown by PLD Technique for Optoelectronics. *Mater. Sci. Semicond. Process.* **2017**, *71*, 378−381.

(60) Sudrajat, H.; Hartuti, S. Boosting Electron Population in δ-Bi_2O_3 through Iron Doping for Improved Photocatalytic Activity. *Adv. Powder Technol.* **2019**, *30*, 983−991.

(61) Ayhan, Y. S.; Buyukaksoy, A. Impact of Fabrication Temperature on the Stability of Yttria Doped Bismuth Oxide Ceramics. *Solid State Ionics* **2019**, *338*, 66−73.

(62) Wu, Y.-C.; Chang, Y.-W.; Wang, S.-F. Electrical Properties and Microstructural Analysis of Aliovalent-Ion (Y^{3+}, Nb^{5+})−Doped Bismuth-Based Solid-Oxide Electrolyte. *Ferroelectrics* **2013**, *455*, 123−128.

(63) Depablos-Rivera, O.; Rodil, S. E. Structural Stabilization and Ionic Conductivity of Bismuth Niobium Oxide Films with Fluorite-Like Structure. *Mater. Lett.* **2020**, *267*, No. 127540.

(64) Kikuchi, T.; Kitami, Y.; Yokoyama, M.; Sakai, H. Pseudo-Binary System Bi_2O_3-TeO_2 in Air. *J. Mater. Sci.* **1989**, *24*, 4275−4278.

(65) Lin, S. E.; Wei, W. C. J. Long-Term Degradation of Ta_2O_5-Doped Bi_2O_3 Systems. *J. Eur. Ceram. Soc.* **2011**, *31*, 3081−3086.

(66) Bourja, L.; Bakiz, B.; Benlhachemi, A.; Ezahri, M.; Valmalette, J. C.; Villain, S.; Gavarri, J.-R. Structural and Raman Vibrational Studies of CeO_2-Bi_2O_3 Oxide System. *Adv. Mater. Sci. Eng.* **2009**, *2009*, No. 502437.

(67) Bourja, L.; Bakiz, B.; Benlhachemi, A.; Ezahri, M.; Villain, S.; Crosnier, O.; Favotto, C.; Gavarri, J.-R. Structural, Microstructural and Surface Properties of a Specific CeO_2-Bi_2O_3 Multiphase System Obtained at 600 °C. *J. Solid State Chem.* **2011**, *184*, 608−614.

(68) Bourja, L.; Bakiz, B.; Benlhachemi, A.; Ezahri, M.; Villain, S.; Favotto, C.; Gavarri, J.-R. Electrical Properties of a CeO_2-Bi_2O_3 Mix System Elaborated at 600 °C. *Adv. Mater. Sci. Eng.* **2012**, *2012*, No. 452383.

(69) Huang, Y.; Zhou, G.; Wei, D.; Fan, Z.; Seo, H. J. Phase-Formation and Luminescence Properties of Eu^{3+}-Doped Bi_2O_3 on Synthetic Process. *J. Lumin.* **2020**, *220*, No. 116970.

(70) Kalaycioglu, N. O.; Çırçır, E. Measurement and Properties of the Oxide Ionic Conductivity of β- and δ-Phases in the Binary $(Bi_2O_3)_{1-x}(Tb_4O_7)_x$ System. *Synth. React. Inorg. Met. Org. Nano. Met. Chem.* **2012**, *42*, 398−401.

(71) Bandyopadhyay, S.; Dutta, A. Thermal, Optical and Dielectric Properties of Phase Stabilized δ − Dy-Bi_2O_3 Ionic Conductors. *J. Phys. Chem. Solids* **2017**, *102*, 12−20.

(72) Li, R.; Zhen, Q.; Drache, M.; Rubbens, A.; Estournes, C.; Vannier, R.-N. Synthesis and Ion Conductivity of

$(Bi_2O_3)_{0.75}(Dy_2O_3)_{0.25}$ Ceramics with Grain Sizes from the Nano to the Micro Scale. *Solid State Ionics* **2011**, *198*, 6−15.

(73) Concha-Balderrama, A.; Martinez-Rodriguez, H. A.; Rojas-George, G.; Esparza-Ponce, H. E.; Orozco-Carmona, V.; Pizá-Ruiz, P.; Bocanegra-Bernal, M. H.; Reyes-Rojas, A. Enhanced Ionic Transport and Compressive Residual Stress in Er-Doped Bi_2O_3 with Lower Er^{3+} Concentrations. *J. Electron. Mater.* **2018**, *47*, 5422−5432.

(74) Duan, N.; Ma, J.; Li, J.; Yan, D.; Chi, B.; Pu, J.; Li, J. High Performance Cathode - Unsintered Solid Oxide Fuel Cell Enhanced by Porous $Bi_{1.6}Er_{0.4}O_3$ (ESB) Interlayer. *Int. J. Hydrogen Energy* **2018**, *43*, 12713−12719.

(75) Kąc, S.; Szwachta, G.; Cieniek, Ł.; Moskalewicz, T. Morphology and Structure of the Erbium Stabilized Bismuth Oxide Thin Films Deposited by PLD Technique. *Arch. Metall. Mater.* **2019**, *64*, 969−974.

(76) Dapčević, A.; Poleti, D.; Rogan, J.; Radojković, A.; Radović, M.; Branković, G. A New Electrolyte Based on Tm^{3+}-Doped δ-Bi_2O_3-Type Phase with Enhanced Conductivity. *Solid State Ionics* **2015**, *280*, 18−23.

(77) Kalaycioglu, N. O.; Öztürk, E.; Dayan, S. Oxide Ionic Conductivity Properties of Binary δ-$(Bi_2O_3)_{1-x}(Yb_2O_3)_x$ System. *J. Chin. Adv. Mater. Soc.* **2013**, *1*, 74−80.

(78) Ozlu Torun, H.; Cakar, S.; Ersoy, E.; Turkoglu, O. The Bulk Electrical Conductivity Properties of δ-Bi_2O_3 Solid Electrolyte System Doped with Yb_2O_3. *J. Therm. Anal. Calorim.* **2015**, *122*, 525−536.

(79) Öztürk, E.; Kalaycioglu, N. O. Synthesis, Characterization and Oxide Ionic Conductivity of Binary δ-$(Bi_2O_3)_{1-x}(Lu_2O_3)_x$ System. *J. Chin. Chem. Soc.* **2013**, *60*, 605−607.

(80) Meenakshi, P.; Promila, K.; Sitharaman, U.; Nagarajan, R. Evaluation of Solid Solution Formation between ThO_2 and δ-Bi_2O_3 by Molecular Precursor Route. *Mater. Res. Bull.* **2018**, *107*, 66−73.

(81) Zdujic, M.; Poleti, D.; Jovalekic, C.; Karanovic, L. Mechanochemical Synthesis and Electrical Conductivity of Nanocrystalline δ-Bi_2O_3 Stabilized by HfO_2 and ZrO_2. *J. Serb. Chem. Soc.* **2009**, *74*, 1401−1411.

(82) Zhou, G.; Huang, Y.; Wei, D.; Bi, S.; Seo, H. J. Preparation and Optical Properties of Te^{4+}/V^{5+}-Stabilized δ-Bi_2O_3 for Visible Light-Driven Photocatalyst. *Mater. Des.* **2019**, *181*, No. 108066.

(83) Leszczynska, M.; Borowska-Centkowska, A.; Malys, M.; Dygas, J. R.; Krok, F.; Wrobel, W.; Abrahams, I. The Double Rare-Earth Substituted Bismuth Oxide System $Bi_3Y_{1-x}Yb_xO_6$. *Solid State Ionics* **2015**, *269*, 37−43.

(84) Chou, T.; Liu, L.-D.; Wei, W.-C. J. Phase Stability and Electric Conductivity of $Er_2O_3-Nb_2O_5$ Co-Doped Bi_2O_3 Electrolyte. *J. Eur. Ceram. Soc.* **2011**, *31*, 3087−3094.

(85) Yilmaz, S.; Celen, C. Synthesis and Microstructural Characterization of δ-Phase Bismuth-Based Electroceramic Systems by Double-Doping Regime. *Int. J. Appl. Ceram. Technol.* **2018**, *15*, 391−398.

(86) Çorumlu, V.; Ermiş, İ.; Acer, S. D.; Çifci, T.; Dağdemir, Y.; Ari, M. The Phase Stability and Conductivity of $Ho_2O_3-Gd_2O_3$ Co-Doped Electrolyte for Solid Oxide Fuel Cell. *J. Mater. Sci.-Mater. Med.* **2016**, *27*, 5839−5845.

(87) Kaşikci Özen, M.; Kayali, R.; Çiçek Bezir, N.; Evcin, A. Synthesizing of $(Bi_2O_3)_{1-x-y}(Ho_2O_3)_x(Dy_2O_3)_y$ Electrolytes for Intermediate-Temperature Solid Oxide Fuel Cells. *Acta Phys. Pol. A* **2016**, *129*, 125−132.

(88) Jung, D. W.; Duncan, K. L.; Wachsman, E. D. Effect of Total Dopant Concentration and Dopant Ratio on Conductivity of $(DyO_{1.5})_x-(WO_3)_y-(BiO_{1.5})_{1-x-y}$. *Acta Mater.* **2010**, *58*, 355−363.

(89) Polat, Y.; Arı, M.; Dağdemir, Y. Phase Stability, Thermal, Electrical and Structural Properties of $(Bi_2O_3)_{1-x-y}(Sm_2O_3)_x(CeO_2)_y$ Electrolytes for Solid Oxide Fuel Cells. *Phase Transitions* **2017**, *90*, 387−398.

(90) Kayalı, R.; Özen, M. K.; Bezir, N. Ç.; Evcin, A. Effect of Concentration of Sm_2O_3 and Yb_2O_3 and Synthesizing Temperature on Electrical and Crystal Structure of $(Bi_2O_3)_{1-x-y}(Sm_2O_3)_x(Yb_2O_3)_y$ Electrolytes Fabricated for IT-SOFCs. *Phys. B* **2016**, *489*, 39−44.

(91) Orlova, E. I.; Kharitonova, E. P.; Gorshkov, N. V.; Goffman, V. G.; Voronkova, V. I. Phase Formation and Electrical Properties of Bi_2O_3-Based Compounds in the Bi_2O_3-La_2O_3-MoO_3 System. *Solid State Ionics* **2017**, *302*, 158−164.

(92) Kharitonova, E. P.; Orlova, E. I.; Gorshkov, N. V.; Goffman, V. G.; Voronkova, V. I. Stabilized Bi_2O_3-Based Phases in the $Bi_2O_3-Pr_2O_3-MoO_3$ System and Their Electrical Properties. *Ceram. Int.* **2018**, *44*, 12886−12895.

(93) Kış, M.; Polat, Y.; Erdoğan, B.; Arı, M. New Fabricated Electrolytes Based on Dy^{3+}-Tm^{3+} Double-Doped δ-Bi_2O_3-Type Cubic Phase. *J. Aust. Ceram. Soc.* **2020**, *56*, 987.

(94) Polat, Y.; Akalan, H.; Arı, M. Thermo-Electrical and Structural Properties of Gd_2O_3 and Lu_2O_3 Double-Doped Bi_2O_3. *Int. J. Hydrogen Energy* **2017**, *42*, 614−622.

(95) Polat, Y.; Arı, M.; Dağdemir, Y. Magnetic Properties of Co-doped Bismuth Oxide (δ-Bi_2O_3) at Low Temperature. *J. Low Temp. Phys.* **2018**, *193*, 74−84.

(96) Yilmaz, S.; Kavici, B.; Celen, C.; Yildiz, E.; Gurbuz, A. Structure and Conductivity Characterization of New Type Ionic Conductor Stabilized Bismuth Oxide Ternary Systems. *Chinese J. Phys.* **2018**, *56*, 362−373.

(97) Yilmaz, S.; Yildiz, E.; Kavici, B. Fabrication, Characterization, and Performance of YbDSB Ternary Compounds for IT-SOFC Applications. *Int. J. Appl. Ceram. Technol.* **2017**, *14*, 550−561.

(98) Sethi, A.; Pandey, J.; Uma, S.; Nagarajan, R. Luminescence Properties of Eu^{3+}- and Tb^{3+}-doped δ-Bi_2O_3 Stabilized by Th^{4+} Substitution. *J. Am. Ceram. Soc.* **2020**, *103*, 1027−1036.

(99) Francesconi, M. G.; Kirbyshire, A. L.; Greaves, C.; Richard, O.; Van Tendeloo, G. Synthesis and Structure of $Bi_{14}O_{20}(SO_4)$, A New Bismuth Oxide Sulfate. *Chem. Mater.* **1998**, *10*, 626−632.

(100) Warda, S. A.; Pietzuch, W.; Massa, W.; Kesper, U.; Reinen, D. Color and Constitution of Cr^{VI}-Doped Bi_2O_3 Phases: The Structure of $Bi_{14}CrO_{24}$. *J. Solid State Chem.* **2000**, *149*, 209−217.

(101) Crumpton, T. E.; Francesconi, M. G.; Greaves, C. The Structural Chemistry of $Bi_{14}MO_{24}$ (M = Cr, Mo, W) Phases: Bismuth Oxides Containing Discrete MO_4 tetrahedra. *J. Solid State Chem.* **2003**, *175*, 197−206.

(102) Crumpton, T. E.; Mosselmans, J. F. W.; Greaves, C. Structure and Oxide Ion Conductivity in $Bi_{28}Re_2O_{49}$, A New Bismuth Rhenium Oxide Containing Tetrahedral and Octahedral Re(VII). *J. Mater. Chem.* **2005**, *15*, 164−167.

(103) Zhou, W. Z. Defect Fluorite Superstructures in the Bi_2O_3-WO_3 System. *J. Solid State Chem.* **1994**, *108*, 381−394.

(104) Hoda, S. N.; Chang, L. L. Y. Phase Relations in the System Bi_2O_3-WO_3. *J. Am. Ceram. Soc.* **1974**, *57*, 323−326.

(105) Bryzgalova, A. N.; Matskevich, N. I.; Greaves, C.; Hervoches, C. H. Formation Enthalpies and Thermodynamics of Some Reactions of the $Bi_{12.5}R_{1.5}ReO_{24.5}$ (R = Y, Nd, La) Compounds. *Thermochim. Acta* **2011**, *513*, 124−127.

(106) Hervoches, C. H.; Greaves, C. Crystal Structure and Oxide Ion Conductivity in Cubic (Disordered) and Tetragonal (Ordered) Phases of $Bi_{25}Ln_3Re_2O_{49}$ (Ln = La, Pr). *J. Mater. Chem.* **2010**, *20*, 6759−6763.

(107) Matskevich, N. I.; Wolf, T.; Bryzgalova, A. N.; Chupakhina, T. I.; Zolotova, E. S.; Matskevich, M. Y.; Bespyatov, M. A. Thermochemical Investigation of δ-Bi_2O_3 Doped by Re_2O_7 and Sm_2O_3. *Thermochim. Acta* **2014**, *575*, 17−20.

(108) Matskevich, N. I.; Bryzgalova, A. N.; Wolf, T.; Adelmann, P.; Ernst, D.; Chupakhina, T. I. Thermochemical Investigation of the New Phase $Bi_{12.5}Gd_{1.5}ReO_{24.5}$. *J. Chem. Thermodyn.* **2012**, *53*, 23−26.

(109) Matskevich, N. I.; Wolf, T. Calorimetric Investigation of New $Bi_{12.5}Dy_{1.5}ReO_{24.5}$ Phase. *J. Alloys Compd.* **2012**, *538*, 45−47.

(110) Matskevich, N. I.; Wolf, T.; Adelmann, P.; Bryzgalova, A. N. Thermodynamic Characteristics of a New Phase $Bi_{12.5}Ho_{1.5}ReO_{24.5}$ by Solution Calorimetry. *J. Alloys Compd.* **2014**, *604*, 325−326.

(111) Punn, R.; Gameson, I.; Berry, F.; Greaves, C. The Local Environment of Cations in $Bi_{12.5}Er_{1.5}ReO_{24.5}$. *J. Phys. Chem. Solids* **2008**, *69*, 2687−2690.

(112) Hervoches, C. H.; Greaves, C. Variable Temperature Neutron Diffraction Study of Crystal Structure and Transport Pathways in

Oxide Ion Conductors $Bi_{12.5}Ln_{1.5}ReO_{24.5}$ (Ln=Lu, Er). *Solid State Ionics* **2014**, *254*, 1−5.

(113) Matskevich, N. I.; Wolf, T.; Greaves, C.; Adelmann, P.; Vyazovkin, I. V.; Matskevich, M. Y. New Phases $Bi_{12.5}Ln_{1.5}ReO_{24.5}$: Thermodynamics and Influence of Dopant Size on Lattice Energy (Ln - Lanthanide). *J. Chem. Thermodyn.* **2015**, *91*, 234−239.

(114) Matskevich, N. I.; Wolf, T.; Pischur, D.; Kozlova, S. G. The Heat Capacity and Thermodynamic Functions of $Bi_{12.5}Lu_{1.5}ReO_{24.5}$ in the Temperature Range of 175−550 K. *J. Therm. Anal. Calorim.* **2016**, *124*, 1745−1748.

(115) Matskevich, N. I.; Wolf, T.; Greaves, C.; Bryzgalova, A. N. Preparation, Ionic Conductivity and Thermochemistry of New $Bi_{12.5}Lu_{1.5}ReO_{24.5}$ Phase. *J. Alloys. Compd.* **2014**, *582*, 253−256.

(116) Crumpton, T. E.; Greaves, C. The Structural Chemistry and Oxide Ion Conducting Properties of the New Bismuth Oxide Sulfate, $Bi_8O_{11}(SO_4)$. *J. Mater. Chem.* **2004**, *14*, 2433−2437.

(117) Smirnov, V. I.; Ponomareva, V. G.; Yukhin, Y. M.; Uvarov, N. F. Fluorite-Related Phases in the Bi_2O_3-SO_3 System. *Solid State Ionics* **2003**, *156*, 79−84.

(118) Weber, M.; Schlesinger, M.; Walther, M.; Zahn, D.; Schalley, C. A.; Mehring, M. Investigations on the Growth of Bismuth Oxido Clusters and the Nucleation to Give Metastable Bismuth Oxide Modifications. *Z. Krist.-Cryst. Mater.* **2017**, *232*, 185−207.

(119) Miersch, L.; Rüffer, T.; Mehring, M. Organic-Inorganic Hybrid Materials Starting from the Novel Nanoscaled Bismuth Oxido Methacrylate Cluster $[Bi_{38}O_{45}(OMc)_{24}(DMSO)_9]\cdot 2DMSO\cdot 7H_2O$. *Chem. Commun.* **2011**, *47*, 6353−6355.

(120) Weber, M.; Schlesinger, M.; Mehring, M. Evaluation of Synthetic Methods for Bismuth(III) Oxide Polymorphs: Formation of Binary versus Ternary Oxides. *Cryst. Growth Des.* **2016**, *16*, 5678−5688.

(121) Weber, M.; Rodriguez, R. D.; Zahn, D. R. T.; Mehring, M. γ-Bi_2O_3 − To Be or Not To Be? Comparison of the Sillenite γ-Bi_2O_3 and Isomorphous Sillenite-Type $Bi_{12}SiO_{20}$. *Inorg. Chem.* **2018**, *57*, 8540−8549.

(122) Coelho, A. A. Whole-Profile Structure Solution from Powder Diffraction Data using Simulated Annealing. *J. Appl. Crystallogr.* **2000**, *33*, 899−908.

(123) Tauc, J.; Grigorovici, R.; Vancu, A. Optical Properties and Electronic Structure of Amorphous Germanium. *Phys. Status Solidi B* **1966**, *15*, 627−637.

(124) Davis, E. A.; Mott, N. F. Conduction in Non-Crystalline Systems V. Conductivity, Optical Absorption and Photoconductivity in Amorphous Semiconductors. *Philos. Mag. A* **1970**, *22*, 0903−0922.

(125) Viezbicke, B. D.; Patel, S.; Davis, B. E.; Birnie, D. P. Evaluation of the Tauc Method for Optical Absorption Edge Determination: ZnO Thin Films as a Model System. *Phys. Status Solidi B* **2015**, *252*, 1700−1710.

(126) Xu, C.; Zhao, P.; Cai, M.; Dan, Z.; Zeng, S.; Du, J.; Yang, P.; Xiong, J. Enhanced Photocatalytic Reduction of Cr(VI) by Cu_2O/Bi_5O_7I Microrods Composites under Visible Light. *J. Photochem. Photobiol. A Chem.* **2020**, *395*, No. 112495.

(127) Zhou, M.; Wu, J.; Wang, H.; Guan, D.; Dong, X.; Wang, J.; Jia, T.; Liu, Q. Fabrication of Z-Scheme Heterojunction g-C_3N_4/Yb^{3+}-Bi_5O_7I Photocatalysts with Enhanced Photocatalytic Performance under Visible Irradiation for Hg^0 Removal. *Energy Fuel.* **2020**, *34*, 16445−16455.

(128) Kubelka, P.; Munk, F. Ein Beitrag zur Optik der Farbanstriche. *Z. Techn. Phys.* **1931**, *12*, 593−601.

(129) López, R.; Gómez, R. Band-Gap Energy Estimation from Diffuse Reflectance Measurements on Sol−Gel and Commercial TiO_2: A Comparative Study. *J. Sol. Gel. Sci. Technol.* **2012**, *61*, 1−7.

(130) Makuła, P.; Pacia, M.; Macyk, W. How To Correctly Determine the Band Gap Energy of Modified Semiconductor Photocatalysts Based on UV−Vis Spectra. *J. Phys. Chem. Lett.* **2018**, *9*, 6814−6817.

(131) Hofmann, M.; Rößner, L.; Armbrüster, M.; Mehring, M. Thin Coatings of α- and β-Bi_2O_3 by Ultrasonic Spray Coating of a Molecular Bismuth Oxido Cluster and their Application for Photocatalytic Water Purification Under Visible Light. *ChemistryOpen* **2020**, *9*, 277−284.

(132) Battle, P. D.; Catlow, C. R. A.; Drennan, J.; Murray, A. D. The Structural Properties of the Oxygen Conducting δ Phase of Bi_2O_3. *J. Phys. C Solid State Phys.* **1983**, *16*, L561−L566.

(133) Yashima, M.; Ishimura, D. Crystal Structure and Disorder of the Fast Oxide-Ion Conductor Cubic Bi_2O_3. *Chem. Phys. Lett.* **2003**, *378*, 395−399.

(134) Willis, B. T. M. Neutron Diffraction Studies of Actinide Oxides. II. Thermal Motions of Atoms in Uranium Dioxide and Thorium Dioxide between Room Temperature and 1100 °C. *P. Roy. Soc. Lond. A Mater.* **1963**, *274*, 134−144.

(135) Willis, B. T. M. Structures of UO_2, UO_{2+x} and U_4O_9 by Neutron Diffraction. *J. Phys.-Paris* **1964**, *25*, 431−439.

(136) Willis, B. T. M. The Anomalous Behaviour of Neutron Reflexions of Fluorite. *Acta Crystallogr.* **1965**, *18*, 75−76.

(137) Blower, S. K.; Greaves, C. The Structure of β-Bi_2O_3 from Powder Neutron-Diffraction Data. *Acta Crystallogr. C* **1988**, *44*, 587−589.

(138) Shannon, R. D. Revised Effective Ionic-Radii and Systematic Studies of Interatomic Distances in Halides and Chalcogenides. *Acta Crystallogr. A* **1976**, *32*, 751−767.

(139) Nakamoto, K.; Fujita, J.; Tanaka, S.; Kobayashi, M. Infrared Spectra of Metallic Complexes. IV. Comparison of the Infrared Spectra of Unidentate and Bidentate Metallic Complexes. *J. Am. Chem. Soc.* **1957**, *79*, 4904−4908.

(140) de Saja, A. G.; Rull, F.; Pastor, J. M.; de Saja, J. A. Infrared and Raman Spectra of Cerium Selenate Pentahydrate. *Spectrochim. Acta* **1986**, *42*, 997−999.

(141) Fries, T.; Lang, G.; KemmlerSack, S. Defect Fluorite Structures in the Bi-Rich Part of the System Bi_2O_3-Re_2O_7. *Solid State Ionics* **1996**, *89*, 233−240.

(142) Baran, E. J. The Vibrational Spectrum of $Ba_5(ReO_6)_2$. *Monatsh. Chem.* **1976**, *107*, 1327−1333.

(143) Sathianandan, K.; McCory, L. D.; Margrave, J. L. Infrared Absorption Spectra of Inorganic Solids - III Selenates and Selenites. *Spectrochim. Acta* **1964**, *20*, 957−963.

(144) Khandelwal, B. L.; Verma, V. P. Liquid-Liquid Distribution, Spectrophotometric, Thermal, IR and Raman Studies in Selenito Uranylates. *J. Inorg. Nucl. Chem.* **1976**, *38*, 763−769.

(145) Newman, G.; Powell, D. B. The Infra-Red Spectra and Structures of Metal-Sulphite Compounds. *Spectrochim. Acta* **1963**, *19*, 213−224.

(146) Lazarević, Z.; Kostić, S.; Radojević, V.; Romčević, M.; Gilić, M.; Petrović-Damjanović, M.; Romčević, N. Raman Spectroscopy of Bismuth Silicon Oxide Single Crystals Grown by the Czochralski Technique. *Phys. Scr.* **2013**, *T157*, No. 014046.

(147) Hardcastle, F. D.; Wachs, I. E. The Molecular Structure of Bismuth Oxide by Raman Spectroscopy. *J. Solid State Chem.* **1992**, *97*, 319−331.

(148) Sekar, G.; Ramakrishnan, V.; Aruldhas, G. IR and Polarized Raman Spectra of $(NH_4)_2M(SO_4)_2\cdot 6H_2O$ (M = Zn, Mn). *J. Solid State Chem.* **1988**, *74*, 424−427.

(149) Bushiri, M. J.; Antony, C. J.; Fleck, M. Raman and infrared spectral studies of $[C(NH_2)_3]_2M^{II}(H_2O)_4(SO_4)_2$, M^{II} = Mn, Cd and VO. *J. Raman Spectrosc.* **2008**, *39*, 368−373.

(150) Frost, R. L.; Čejka, J.; Dickfos, M. J. Raman Spectroscopic Study of the Uranyl Selenite Mineral Demesmaekerite $Pb_2Cu_5(UO_2)_2(SeO_3)_6(OH)_6\cdot 2H_2O$. *J. Raman Spectrosc.* **2009**, *40*, 476−480.

(151) Frost, R. L.; Keeffe, E. C. Raman Spectroscopic Study of the Selenite Minerals - Chalcomenite $CuSeO_3\cdot 2H_2O$ Clinochalcomenite and Cobaltomenite. *J. Raman Spectrosc.* **2008**, *39*, 1789−1793.

(152) Frost, R. L.; Keeffe, E. C. Raman Spectroscopic Study of the Selenite Mineral: Ahifeldite, $NiSeO_3\cdot 2H_2O$. *J. Raman Spectrosc.* **2009**, *40*, 509−512.

(153) Raimbault, G.; Romain, F.; Lautié, A. Raman and Infrared Study of Structural Phase-Transitions in $(NH_4)_3H(SeO_4)_2$ and $(ND_4)_3D(SeO_4)_2$. *J. Raman Spectrosc.* **1992**, *23*, 147−154.

(154) Hardcastle, F. D.; Wachs, I. E.; Horsley, J. A.; Via, G. H. The Structure of Surface Rhenium Oxide on Alumina from Laser Raman Spectroscopy and X-Ray Absorption Near-Edge Spectroscopy. *J. Mol. Catal.* **1988**, *46*, 15−36.

(155) Gassman, P. L.; McCloy, J. S.; Soderquist, C. Z.; Schweiger, M. J. Raman Analysis of Perrhenate and Pertechnetate in Alkali Salts and Borosilicate Glasses. *J. Raman Spectrosc.* **2014**, *45*, 139−147.

(156) Müller, A. Faktorgruppenanalyse der optischen Schwingungen von $KReO_4$ im Raman-Effekt und im Infrarotspektrum[1, 2]. *Z. Naturforsch. A* **1966**, *21*, 433−436.

(157) Kemmler-Sack, S.; Jooss, I.; Cyris, W.-R.; Fadini, A. Vibrational Spectroscopic Investigations on the Ordered Perovskites $A_2^{II}B^{I}Re^{VII}O_6$. *Z. Anorg. Allg. Chem.* **1979**, *453*, 153−156.

(158) Ortiz-Quiñonez, J.-L.; Díaz, D.; Zumeta-Dubé, I.; Arriola-Santamaría, H.; Betancourt, I.; Santiago-Jacinto, P.; Nava-Etzana, N. Easy Synthesis of High-Purity $BiFeO_3$ Nanoparticles: New Insights Derived from the Structural, Optical, and Magnetic Characterization. *Inorg. Chem.* **2013**, *52*, 10306−10317.

(159) Rea, D. G. On the Theory of the Resonance Raman Effect. *J. Mol. Spectrosc.* **1960**, *4*, 499−506.

(160) Albrecht, A. C. Theory of Raman Intensities. *J. Chem. Phys.* **1961**, *34*, 1476−1484.

(161) Zayed, H. A. Physical Properties of δ-Bi_2O_3 Thin Films. *Fizika A* **1995**, *4*, 45−53.

(162) Fan, H. T.; Teng, X. M.; Pan, S. S.; Ye, C.; Li, G. H.; Zhang, L. D. Optical Properties of δ-Bi_2O_3 Thin Films Grown by Reactive Sputtering. *Appl. Phys. Lett.* **2005**, *87*, No. 231916.

(163) Fan, H. T.; Pan, S. S.; Teng, X. M.; Ye, C.; Li, G. H. Structure and Thermal Stability of δ-Bi_2O_3 Thin Films Deposited by Reactive Sputtering. *J. Phys. D: Appl. Phys.* **2006**, *39*, 1939−1943.

(164) Huang, R. Z.; Wei, Y. Y.; Gao, T. F.; Li, C. M.; Jiang, C. H. Structure and Electronic Properties of δ-Bi_2O_3 Tuned by Vacancy and Doping: A First-Principles Study. *Ceram. Int.* **2021**, *47*, 205−213.

(165) Taylor, P.; Sunder, S.; Lopata, V. J. Structure, Spectra, and Stability of Solid Bismuth Carbonates. *Can. J. Chem.* **1984**, *62*, 2863−2873.

(166) Lee, E. P.; Song, S. Y.; Lee, D. W.; Ok, K. M. New Bismuth Selenium Oxides: Syntheses, Structures, and Characterizations of Centrosymmetric $Bi_2(SeO_3)_2(SeO_4)$ and $Bi_2(TeO_3)_2(SeO_4)$ and Noncentrosymmetric $Bi(SeO_3)(HSeO_3)$. *Inorg. Chem.* **2013**, *52*, 4097−4103.

(167) Rademacher, O.; Göbel, H.; Ruck, M.; Opperman, H. Crystal Structure of Dibismuth Selenium Pentoxide, Bi_2SeO_5. *Z. Krist.-New Cryst. St.* **2001**, *216*, 29−30.

(168) Bontschewa-Mladenova, Z.; Georgiew, G. Synthesis and Thermostability of Antimony and Bismuth Chalcogenates. 4. Studies on Synthesis and Thermostability of Bismuth Selenate. *Monatsh. Chem.* **1975**, *106*, 283−289.

(169) Weber, M.; Schlesinger, M.; Mehring, M. Evaluation of Synthetic Methods for Bismuth(III) Oxide Polymorphs: Formation of Binary versus Ternary Oxides. *Cryst. Growth Des.* **2016**, *16*, 5678−5688.

(170) Weber, M.; Rodriguez, R. D.; Zahn, D. R. T.; Mehring, M. γ-Bi_2O_3 − To Be or Not To Be? Comparison of the Sillenite γ-Bi_2O_3 and Isomorphous Sillenite-Type $Bi_{12}SiO_{20}$. *Inorg. Chem.* **2018**, *57*, 8540−8549.

(171) Nestmann, E. R.; Douglas, G. R.; Matula, T. I.; Grant, C. E.; Kowbel, D. J. Mutangenic Activity of Rhodamine Dyes and Their Impurities as Detected by Mutation Induction in Salmonella and DNA Damage in Chinese Hamster Ovary Cells. *Cancer Res.* **1979**, *39*, 4412−4417.

(172) Lewis, I. L.; Patterson, R. M.; McBay, H. C. The Effects of Rhodamine B on the Chromosomes of *Muntiacus Muntjac*. *Mutat. Res.* **1981**, *88*, 211−216.

(173) Evans, N. A. Photofading of Rhodamine Dyes I - Identification of Some Rhodamine B Photoproducts. *J. Soc. Dyers Colour.* **1970**, *86*, 174−177.

(174) Evans, N. A. Photofading of Rhodamine Dyes: III. The Effect of Wavelength on the Fading of Rhodamine B. *Text. Res. J.* **1973**, *43*, 697−700.

(175) Ma, Y.; Yao, J. N. Photodegradation of Rhodamine B Catalyzed by TiO_2 Thin Films. *J. Photochem. Photobiol. A* **1998**, *116*, 167−170.

(176) Park, H.; Choi, W. Photocatalytic Reactivities of Nafion-Coated TiO_2 for the Degradation of Charged Organic Compounds under UV or Visible Light. *J. Phys. Chem. B* **2005**, *109*, 11667−11674.

(177) Pichat, P. *Photocatalysis and Water Purification: From Fundamentals to Recent Applications*; Wiley-VCH Verlag GmbH & Co. KGaA: 2013.

(178) Merka, O.; Yarovyi, V.; Bahnemann, D. W.; Wark, M. pH-Control of the Photocatalytic Degradation Mechanism of Rhodamine B over $Pb_3Nb_4O_{13}$. *J. Phys. Chem. C* **2011**, *115*, 8014−8023.

(179) Watanabe, T.; Takizawa, T.; Honda, K. Photocatalysis Through Excitation of Adsorbates. 1. Highly Efficient N-Deethylation of Rhodamine B Adsorbed to CdS. *J. Phys. Chem.* **1977**, *81*, 1845−1851.

(180) Qu, P.; Zhao, J. C.; Shen, T.; Hidaka, H. TiO_2-Assisted Photodegradation of Dyes: A Study of Two Competitive Primary Processes in the Degradation of RB in an Aqueous TiO_2 Colloidal Solution. *J. Mol. Catal. A-Chem.* **1998**, *129*, 257−268.

(181) Fox, M. A.; Dulay, M. T. Heterogeneous Photocatalysis. *Chem. Rev.* **1993**, *93*, 341−357.

(182) Saison, T.; Chemin, N.; Chanéac, C.; Durupthy, O.; Ruaux, V.; Mariey, L.; Maugé, F.; Beaunier, P.; Jolivet, J. P. Bi_2O_3, $BiVO_4$, and Bi_2WO_6: Impact of Surface Properties on Photocatalytic Activity under Visible Light. *J. Phys. Chem. C* **2011**, *115*, 5657−5666.

(183) Chen, F.; Zhao, J. C.; Hidaka, H. Highly Selective Deethylation of Rhodamine B: Adsorption and Photooxidation Pathways of the Dye on the TiO_2/SiO_2 Composite Photocatalyst. *Int. J. Photoenergy* **2003**, *5*, 209−217.

(184) Eberl, J.; Kisch, H. Visible Light Photo-Oxidations in the Presence of α-Bi_2O_3. *Photochem. Photobiol. Sci.* **2008**, *7*, 1400−1406.

(185) Shi, Y. Y.; Luo, L. J.; Zhang, Y. F.; Chen, Y.; Wang, S.; Li, L. X.; Long, Y. J.; Jiang, F. Z. Synthesis and Characterization of Porous Platelet-Shaped α-Bi_2O_3 with Enhanced Photocatalytic Activity for 17α-Ethynylestradiol. *J. Mater. Sci.* **2018**, *53*, 1049−1064.

(186) Eberl, J.; Kisch, H. Mineralization of Phenol and 4-Chlorophenol Induced by Visible Light and Assisted by Semiconducting β-Bi_2O_3. *Z. Naturforsch. B* **2010**, *65*, 399−404.

(187) Zhang, B.; Peng, X.; Wang, Z. Noble Metal-Free TiO_2-Coated Carbon Nitride Layers for Enhanced Visible Light-Driven Photocatalysis. *Nanomaterials* **2020**, *10*, 805.

(188) Zhou, Z.; Yin, H.; Zhao, Y.; Zhang, J.; Li, Y.; Yuan, J.; Tang, J.; Wang, F. Synthesis of Magnetic α-Fe_2O_3/Rutile TiO_2 Hollow Spheres for Visible-Light Photocatalytic Activity. *Catalysts* **2021**, *11*, 396.

(189) Zhong, C.; Wei, W.; He, H.; Huangfu, Z.; Wang, Y.; Yu, J. The Photocatalytic Performance of Ternary g-$C_3N_4/Bi_2O_3/TiO_2$ Heterojunction Composite for Degradation of Organic Pollutants under Visible and Ultraviolet Light. *J. Mater. Sci. Mater. Med.* **2021**, 32, 2146−2157.

(190) Setiawan, S.; Hardiansyah, A.; Kartikowati, C. W.; Arif, A. F.; Priatmoko, S.; Arutanti, O. Microwave-Assisted Synthesis of TiO_2/GO Composite and Its Adsorption-Photocatalysis Property under Visible Light. *IOP Conf. Ser. Mater. Sci.* **2021**, *1143*, No. 012055.

(191) Dodoo-Arhin, D.; Asiedu, T.; Agyei-Tuffour, B.; Nyankson, E.; Obada, D.; Mwabora, J. M. Photocatalytic Degradation of Rhodamine Dyes using Zinc Oxide Nanoparticles. *Mater. Today Proc.* **2021**, *38*, 809−815.

(192) Yang, X.; Zhang, L.; Wang, D.; Zhang, Q.; Zeng, J.; Zhang, R. Facile Synthesis of Nitrogen-Defective g-C_3N_4 for Superior Photocatalytic Degradation of Rhodamine B. *RSC Adv.* **2021**, *11*, 30503−30509.

(193) Yu, X.; Feng, Q.; Ma, D.; Lin, H.; Liu, Z.; Huang, Y.; Huang, X.; Dong, X.; Lei, Y.; Wang, D. Facile Synthesis of α/β-Bi_2O_3 Hetero-Phase Junction by a Solvothermal Method for Enhanced Photocatalytic Activities. *J. Mol. Catal. A* **2021**, *503*, No. 111431.

(194) Reverberi, A. P.; Varbanov, P. S.; Vocciante, M.; Fabiano, B. Bismuth Oxide-Related Photocatalysts in Green Nanotechnology: A Critical Analysis. *Front. Chem. Sci. Eng.* **2018**, *12*, 878−892.

(195) Weber, M. *Synthese und Charakterisierung von Bismut(III)-basierten Halbleitern ausgehend von homo- und heterometallischen Bismutoxidoclustern*. PhD Thesis, Technische Universität Chemnitz, 2021, https://nbn-resolving.org/urn:nbn:de:bsz:ch1-qucosa2-740796.